



HAL
open science

Adenomatous Polyposis Coli Modulates Actin and Microtubule Cytoskeleton at the Immunological Synapse to Tune CTL Functions

Marie Juzans, Céline Cuche, Thierry Rose, Marta Mastrogiovanni, Pascal Bochet, Vincenzo Di Bartolo, Andrés Alcover

► To cite this version:

Marie Juzans, Céline Cuche, Thierry Rose, Marta Mastrogiovanni, Pascal Bochet, et al.. Adenomatous Polyposis Coli Modulates Actin and Microtubule Cytoskeleton at the Immunological Synapse to Tune CTL Functions. *ImmunoHorizons* , 2020, 4 (6), pp.363-381. 10.4049/immunohorizons.2000044 . pasteur-02975339

HAL Id: pasteur-02975339

<https://pasteur.hal.science/pasteur-02975339>

Submitted on 22 Oct 2020

HAL is a multi-disciplinary open access archive for the deposit and dissemination of scientific research documents, whether they are published or not. The documents may come from teaching and research institutions in France or abroad, or from public or private research centers.

L'archive ouverte pluridisciplinaire **HAL**, est destinée au dépôt et à la diffusion de documents scientifiques de niveau recherche, publiés ou non, émanant des établissements d'enseignement et de recherche français ou étrangers, des laboratoires publics ou privés.



Distributed under a Creative Commons Attribution - NonCommercial 4.0 International License

Adenomatous Polyposis Coli Modulates Actin and Microtubule Cytoskeleton at the Immunological Synapse to Tune CTL Functions

Marie Juzans, Céline Cuche, Thierry Rose, Marta Mastrogiovanni, Pascal Bochet, Vincenzo Di Bartolo and Andrés Alcover

ImmunoHorizons 2020, 4 (6) 363-381

doi: <https://doi.org/10.4049/immunohorizons.2000044>

<http://www.immunohorizons.org/content/4/6/363>

This information is current as of October 22, 2020.

-
- Supplementary Material** <http://www.immunohorizons.org/content/suppl/2020/06/24/4.6.363.DCSupplemental>
- References** This article **cites 58 articles**, 26 of which you can access for free at: <http://www.immunohorizons.org/content/4/6/363.full#ref-list-1>
- Email Alerts** Receive free email-alerts when new articles cite this article. Sign up at: <http://www.immunohorizons.org/alerts>

Adenomatous Polyposis Coli Modulates Actin and Microtubule Cytoskeleton at the Immunological Synapse to Tune CTL Functions

Marie Juzans,^{*,†} Céline Cuche,^{*} Thierry Rose,^{‡,1} Marta Mastrogiovanni,^{*,†} Pascal Bochet,[‡] Vincenzo Di Bartolo,^{*,2} and Andrés Alcover^{*,2}

^{*}Unité Biologie Cellulaire des Lymphocytes, Département d'Immunologie, Institut Pasteur, INSERM-U1221, Ligue Nationale contre le Cancer-Equipe Labellisée Ligue 2018, F-75015 Paris, France; [†]Sorbonne Université, Collège Doctoral, F-75005 Paris, France; and [‡]Bioimage Analysis Unit, Department of Cell Biology and Infection, Institut Pasteur, CNRS-UMR3691, F-75015 Paris, France

ABSTRACT

Adenomatous polyposis coli (Apc) is a cell polarity regulator and a tumor suppressor associated with familial adenomatous polyposis and colorectal cancer. Apc involvement in T lymphocyte functions and antitumor immunity remains poorly understood. Investigating Apc-depleted human CD8 T cells and CD8 T cells from *Apc*^{Min/+} mutant mice, we found that Apc regulates actin and microtubule cytoskeleton remodeling at the immunological synapse, controlling synapse morphology and stability and lytic granule dynamics, including targeting and fusion at the synapse. Ultimately, Apc tunes cytotoxic T cell activity, leading to tumor cell killing. Furthermore, Apc modulates early TCR signaling and nuclear translocation of the NFAT transcription factor with mild consequences on the expression of some differentiation markers. In contrast, no differences in the production of effector cytokines were observed. These results, together with our previous findings on Apc function in regulatory T cells, indicate that Apc mutations may cause a dual damage, first unbalancing epithelial cell differentiation and growth driving epithelial neoplasms and, second, impairing T cell-mediated antitumor immunity at several levels. *ImmunoHorizons*, 2020, 4: 363–381.

Received for publication May 28, 2020. Accepted for publication June 3, 2020.

Address correspondence and reprint requests to: Dr. Vincenzo Di Bartolo and Dr. Andrés Alcover, Lymphocyte Cell Biology Unit, Institut Pasteur, 28 Rue du Dr. Roux, 75724 Paris Cedex 15, France. E-mail addresses: vincenzo.di-bartolo@pasteur.fr (V.D.B.) and andres.alcover@pasteur.fr (A.A.)

ORCIDs: 0000-0001-6085-2473 (M.M.); 0000-0002-5453-947X (V.D.B.); 0000-0002-9507-3450 (A.A.).

¹Current address: Lymphocyte Cell Biology Unit, Department of Immunology, Institut Pasteur, Paris, France.

²Equal contribution as senior authors.

This work was supported by grants from La Ligue Nationale contre le Cancer, Equipe Labellisée 2018, and institutional grants from the Institut Pasteur and INSERM. M.J. was supported by a Ligue Nationale contre le Cancer Doctoral Fellowship and the Institut Pasteur. M.M. is a scholar of the Pasteur Paris University International Doctoral Program, supported by the Institut Pasteur and the European Union Horizon 2020 Research and Innovation Programme under the Marie Skłodowska-Curie grant agreement 665807 (COFUND-PASTEURDOC). The Unit of Technology and Service Photonic Bioluminescence core facility is supported by the French National Research Agency France Bioluminescence (ANR-10-INSB-04, Investments for the Future).

M.J. designed, performed, and analyzed experiments, developed experimental models, and wrote the manuscript; C.C. designed, performed, and analyzed experiments, developed experimental models, and provided technical and laboratory management support; T.R. designed, performed, and analyzed experiments, and developed experimental models. M.M. performed and analyzed some experiments and provided technical support and critical reading. P.B. wrote software for rupture force flow experiments. V.D.B. conceived the project, designed and performed experiments, and wrote the manuscript. A.A. conceived the project, designed experiments, and wrote the manuscript.

Abbreviations used in this article: Apc, adenomatous polyposis coli; ConA, concanavalin A; CV, chamber volume; 3D, three-dimensional; ICAREB, Clinical Investigation and Access to BioResources; shRNA, short hairpin RNA; siApc, siRNA for Apc depletion; siCtrl, siRNA control; siRNA, small interfering RNA; TIRF, total internal reflection fluorescence; Treg, regulatory T cell.

The online version of this article contains supplemental material.

This article is distributed under the terms of the [CC BY-NC 4.0 Unported license](https://creativecommons.org/licenses/by-nc/4.0/).

Copyright © 2020 The Authors

<https://doi.org/10.4049/immunohorizons.2000044>

ImmunoHorizons is published by The American Association of Immunologists, Inc.

INTRODUCTION

TCRs recognize peptide Ags associated with MHC molecules on APCs. Ag interaction induces early TCR signaling, leading to the T cell polarization toward APCs and the formation of the immunological synapse at the T cell Ag-presenting cell interface. Immunological synapses are key to control T cell activation leading to T cell growth, differentiation and cytokine production. They also control T cell effector functions such as polarized secretion of cytokines by Th and regulatory T cells (Tregs) and lytic granules by CTLs (1).

Immunological synapse generation and function depend on the orchestrated action of the actin and microtubule cytoskeleton and of intracellular vesicle traffic that polarize at the T cell side of the immunological synapse. This drives the targeting and dynamic clustering of T cell Ag receptors and signaling molecules to optimally control T cell activation (2). Furthermore, the Golgi and lytic granule intracellular traffic reorient toward the synapse, delivering Th cytokines directly to Ag-presenting B cells (3–5) or lytic granules to infected or tumor target cells. Polarized secretion of lytic granules depends on the fine concomitant dynamic remodeling of actin and microtubule cytoskeleton at the immunological synapse (6–9).

Cell polarity complexes are key to ensure stable cell polarity (10) as well as induced polarization in migrating cells (11). Scribble, Dlg1, and PKC ζ polarity regulators were shown to control lymphocyte migration, immunological synapse formation, and T cell activation (12–17). The polarity regulator and tumor suppressor adenomatous polyposis coli (Apc) is known for its association with familial adenomatous polyposis, human colorectal tumors, and intestinal carcinomas in mice (18–21). Apc interacts with a variety of proteins, including transcription factor regulators as β -catenin, polarity regulators, such as Dlg1 or Scribble, cytoskeleton regulators, such as Cdc42 or EBI1, nuclear pore and nuclear transport proteins, and apoptosis- or mitosis-related proteins (22, 23).

Apc mutations alter intestinal epithelium differentiation and induce tumor progression in colorectal cancer patients and in mouse models (18–22, 24). The role of Apc in immune responses, in particular against tumors, is much less explored. However, altered intestinal immune homeostasis and control of inflammation by Tregs was reported in Apc mutant mice (25–28). We have previously unveiled that Apc underpins various molecular mechanisms controlling CD4 T cell functions (29). These include microtubule network organization and centrosome polarization at the immunological synapse and NFAT-driven cytokine gene activation. Interestingly, Apc regulates NFATc2 nuclear translocation upon T cell activation. Furthermore, NFATc2 forms microclusters associated with microtubules and needs microtubules to translocate to the nucleus upon T cell activation. Finally, in *Apc^{Min/+}* mutant mice, lamina propria Tregs display lower capacity to differentiate and produce cytokines, mainly IL-10 (29). This cytokine is central to regulation of intestinal inflammation and adenocarcinoma progression (30). These findings suggested that Apc mutations may also affect immune cell functions and,

particularly, the anti-inflammatory capacity of Tregs, which could contribute to tumor development in patients carrying Apc mutations.

NFAT is involved in cytotoxic T cell differentiation and function (31). Furthermore, microtubule-mediated lytic granule polarization and release at cytotoxic T cell synapses is crucial for efficient tumor cell killing (7). Therefore, we hypothesized that Apc deficiency might also affect cytotoxic T cell functions, reducing their capacity to eliminate tumor cells and contributing to tumor escape in Apc-dependent polyposis patients. To investigate this, we studied Apc-silenced human primary CD8 T cells and CD8 T cells from *Apc^{Min/+}* mice. These heterozygous mutant mice have been largely used as an animal model to investigate the molecular bases of Apc-mediated intestinal polyposis and carcinoma (19).

In this study, we show that Apc is involved in microtubule and actin cytoskeleton remodeling at the immunological synapse of CD8 T cells. Furthermore, CD8 T cells from *Apc^{Min/+}* mice displayed reduced T cell Ag receptor-mediated Erk and Akt kinase activation and NFAT nuclear translocation. However, mild or no effects were observed on some CD8 differentiation markers or production of cytokines. Importantly, synapse stability, lytic granule dynamics and fusion at the synapse, as well as cytotoxic activity against tumor cells were reduced in ex vivo-differentiated CTLs from *Apc^{Min/+}* mice or from Apc-silenced human CD8 T cells. These results reveal a novel role of Apc in modulating cytotoxic T cell responses, with potential consequences in antitumor immunity.

MATERIALS AND METHODS

Human cell isolation, small interfering RNA transfection, lentiviral infection, CTL generation, and tumor target cell culture

Human peripheral blood T cells from healthy volunteers were obtained from the French Blood Bank Organization (Etablissement Français du Sang) or through the Institut Pasteur Biological Resources Core Facility, Clinical Investigation and Access to BioResources (ICAREB) (NSF 96-900 certified, from sampling to distribution, reference BB-0033-00062/ICAREB platform/Institut Pasteur, Paris, France/BBMRI AO203/1 distribution/access: 2016, May 19th, [BIORESOURCE]), under CoSImmGen protocol approved by the Committee of Protection of Persons, Ile de France-1 (No 2010-dec-12483). Informed consent was obtained from all donors.

PBMCs were isolated by centrifugation through Ficoll-Hypaque. CD8 T cells were isolated from PBMCs using the MACS CD8 T Cell Isolation Kit (Miltenyi Biotec) and maintained in human CD8 medium: RPMI 1640 plus GlutaMAX-I (Life Technologies) supplemented with 10% FBS, 1 mM sodium pyruvate and nonessential amino acids, 10 mM HEPES, 1% penicillin–streptomycin (v/v).

To generate CTLs, freshly isolated CD8 T cells were stimulated 2 d with coated anti-CD3 (10 μ g/ml; UCHT1 produced by A. Alcover), soluble anti-CD28 (7 μ g/ml; Beckman Coulter), and

recombinant human IL-2 (100 U/ml; PeproTech) in human CD8 medium. Cells were infected for 24 h with lentiviruses coding for control or Apc-specific short hairpin RNAs (shRNAs) (10% v/v) in human CD8 medium with IL-2, in which FBS was replaced by human serum and then selected for 3 d with puromycin (3.9 $\mu\text{g/ml}$). The percentage of infected CTLs was 70–85%, as assessed by GFP expression by FACS.

For short interfering RNA (siRNA) experiments, the following small dsRNA oligonucleotide sequence was used for Apc depletion (siRNA for Apc depletion [siApc]: 5'-GAGAAUACGUCCACAC CUU-3' (GE Healthcare), as we previously described (29). As siRNA control (siCtrl), the sequence used was 5'-UAGCGA CUAACACAUCAA-3' (siGENOME Non-Targeting siRNA #1; GE Healthcare). A total of 1×10^7 freshly isolated CD8 T cells were transfected with 1 nmol siCtrl or siApc using the Human T Cell Nucleofactor Kit and the program U-14 on an Amaxa Nucleofactor II (Lonza). Cells were then harvested in human CD8 medium without penicillin–streptomycin and used 72 h after transfection.

For shRNA experiments, lentiviruses were produced by HEK293T cells transfected with the transient calcium phosphate DNA precipitation technique. Cells were transfected with pCMV-deltaR8-2 and pCMV-env-VSV, together with a pLKO.1-puro-CMV-tGFP lentiviral vector expressing or not (as negative control) as shRNA–targeting Apc (5'-GACTGTCCTTTCACCA TATTT-3') (Sigma-Aldrich). Forty-eight hours later, supernatant was recovered and concentrated 40 \times by ultracentrifugation (26,000 rpm, 1.5 h, 4°C). Lentiviruses stocks were stored at -80°C .

The P815 mouse mastocytoma cell line was used as the tumor target cell. P815 cells were maintained in DMEM supplemented with 10% FBS and 1% penicillin–streptomycin (v/v). To make stimulatory target cells, P815 were pulsed with anti-human or mouse CD3 Abs, as described below.

***Apc*^{Min/+} and wild-type mice, lymphocyte isolation, and cell culture**

Heterozygous C57BL/6J-*Apc*^{Min} (*Apc*^{Min/+}) mice and wild-type controls were purchased from The Jackson Laboratory. Mice were housed and bred under pathogen-free conditions in the Central Animal Facility of the Institut Pasteur. The protocols used had been approved by the Ethical Committee for Animal Experimentation of the Institut Pasteur and by the French Ministry of Research. Wild-type and *Apc*^{Min/+} male and female littermates were sacrificed at 8–14 wk of age. The age, gender, and number of mice analyzed per type of experiment are depicted in Supplemental Table I. Individual mice were analyzed separately. We did not observe any significant gender effect in any of the experiments performed. Data from male and female mice were pooled for each experimental condition.

Spleen and lymph nodes were homogenized through a 70- μm filter. To generate CTLs, CD8 T cells were purified using the MACS CD8a T Cell Isolation Kit (Miltenyi Biotec) and stimulated 2 d with coated anti-CD3 (5 $\mu\text{g/ml}$; 145-2C11; eBioscience), soluble anti-CD28 (2 $\mu\text{g/ml}$; eBioscience), and IL-2 (10 ng/ml; Miltenyi Biotec). Cells were then cultured for 5–6 d in mouse CD8 medium: DMEM plus GlutaMAX-I (Life Technologies) supplemented with

10% FBS, 1 mM sodium pyruvate and nonessential amino acids, 50 μM 2-ME, 10 mM HEPES, and 1% penicillin–streptomycin (v/v), in the presence of IL-2 (10 ng/ml; Miltenyi Biotec).

***Apc* quantification**

For Apc detection by Western blot, total cell extracts were obtained by lysing cells for 5 min on ice in lysis buffer (50 mM Tris [pH 7.4], 100 mM NaCl, 0.5% Nonidet P-40, 5 mM EDTA, 5 mM EGTA, 40 mM 2-ME, 10 mM NaF, 10 mM $\text{Na}_4\text{P}_2\text{O}_7$, 2 mM orthovanadate, and protease inhibitor mixture). Cell lysates were cleared by spinning at $20,800 \times g$ for 20 min at 4°C. An equal amount of protein content was measured using the Bio-Rad Protein Assay (Bio-Rad Laboratories) was loaded in NuPAGE 3–8% Tris-Acetate gels (Thermo Fisher Scientific). Proteins were transferred onto nitrocellulose membranes (LI-COR Biosciences) for 4 h using a Bio-Rad Mini Trans-Blot system in buffer containing 50 mM Tris, 380 mM glycine, 20% ethanol, and 0.1% SDS. Membranes were saturated with blocking buffer (Rockland Immunochemicals) and incubated with anti-Apc (2 $\mu\text{g/ml}$; ALi 12–28; Abcam) and anti-ZAP70 (50 ng/ml; BD Biosciences) or anti-PLC γ 1 (1/1000; Cell Signaling Technology) overnight at 4°C. They were washed and then incubated with specific secondary Abs conjugated with Alexa Fluor 680 or DyLight 800 (Thermo Fisher Scientific) for 45 min. Near-infrared fluorescence was imaged and quantified using the Odyssey Classic Near-Infrared Imaging System (LI-COR Biosciences), and the Apc band intensity was normalized to control ZAP70 or PLC γ 1 band.

For Apc detection by retrotranscription quantitative PCR, total RNA was extracted using the RNeasy Plus Micro Kit (QIAGEN) following the manufacturer's instructions. cDNA was obtained from 200 ng of total RNA using an iScript cDNA Synthesis Kit (Bio-Rad Laboratories). FastStart Universal SYBR Green PCR Master Mix (Roche) and an ABI PRISM 7900HT Sequence Detection system (Applied Biosystems) were used to quantify gene products. Quantitative PCR were performed in triplicates. Quantity values were calculated by the relative standard curve method and normalized to the mRNA expression of the *RLP13a* housekeeping gene. The primer sequences used were as follows: Apc forward, 5'-CCAACAAGGCTACGCTATGC-3' and reverse, 5'-TACATCTGCTCGCCAAGACA-3'; RLP13a forward, 5'-CATA GGAAGCTGGGAGCAAG-3' and reverse, 5'-GCCCTCCAAT CAGTCTTCTG-3'

Confocal microscopy, image posttreatment, and quantitative image analysis

Coverslips were washed with HCl–ethanol 70% and coated with poly-L-lysine 0.002% in water (Sigma-Aldrich). For flat pseudosynapse formation, coverslips were further coated with anti-CD3 (10 $\mu\text{g/ml}$; UCHT1; BioLegend) overnight at 4°C. Coverslips were washed and blocked for 30 min at 37°C with human CD8 medium. Human T cells were plated on coverslips for 5 min at 37°C and fixed with 4% paraformaldehyde for 13 min at room temperature. For microtubule detection, cells were also incubated 20 min at -20°C in ice-cold methanol. For CTL–target cell immunological synapse formation, P815 cells, previously coated with anti-CD3

(20 $\mu\text{g}/\text{ml}$; OKT3 produced by A. Alcover) for 45 min at 4°C, were plated on poly-L-lysine-coated coverslips for 15 min at 37°C. Coverslips were carefully washed with PBS, and human CTLs were added at a 1:1 CTL/target ratio and incubated for 15 min at 37°C. Cells were then fixed with 4% paraformaldehyde for 13 min at room temperature. Coverslips were washed in PBS and incubated 1 h in PBS with 1% BSA (v/v) to prevent unspecific binding. Cells were then incubated 1 h at room temperature with PBS, 1% BSA, 0.1% Triton X-100 and anti-Apc (1/300; gift of I. Näthke, University of Dundee), anti- β -tubulin (6.6 $\mu\text{g}/\text{ml}$; Merck Millipore), anti-pericentrin (1/100; Abcam), and anti-perforin (10 $\mu\text{g}/\text{ml}$; BD Biosciences). Coverslips were then incubated with the corresponding fluorescent-coupled secondary Ab and Texas Red-X Phalloidin (1/100; Invitrogen) for 45 min at room temperature. After three washes in PBS with 1% BSA, coverslips were mounted on microscope slides using ProLong Gold Antifade Mountant with DAPI (Life Technologies).

Confocal images were acquired with an LSM 700 confocal microscope (Zeiss) using the Plan Apochromat 63 \times /1.40 numerical aperture objective. Optical confocal sections were acquired with ZEN software (Zeiss) by intercalating green and red laser excitation to minimize channel cross-talk. All analyses were performed using Fiji software (32). For Apc quantification and F-actin analysis, optical sections were acquired at 1- μm intervals. Apc fluorescent intensity was measured on the total cell. Formation of the actin ring and phalloidin fluorescence intensity analyses were performed on one confocal section at the cell-coverslip contact. F-actin intensity profiles were assessed along a line drawn across each cell image (as shown in Fig. 2D). Ranking of each cell in a category (presence of F-actin ring plus central clearance, intermediate; low, F-actin ring plus clearance) was decided after observing actin profiles on three to four different angles. For microtubule pattern and synapses analyses, optical sections were acquired at 0.2- μm intervals, and images were treated by deconvolution with the Huygens Professional software (Scientific Volume Imaging). Microtubule pattern analysis was performed on projection of four confocal sections at the cell-coverslip contact, and phenotypes were classified by blinded image observation by three different investigators. Synapse morphology and cytotoxic granule localization were analyzed in three-dimensional (3D) projections and classified as described for microtubule patterns. Centrosome localization was estimated by measuring the distance between the anti-pericentrin staining and the CTL plasma membrane at the center area of the immunological synapse. Quantification of cytotoxic granules per cell was obtained using the TrackMate plugin for ImageJ developed by J.-Y. Tinevez (Photonic BioImaging, Unit of Technology and Service, Institut Pasteur) (33).

Rupture force assay of cell–cell interactions in laminar flow chamber

Glass surface (Rogo-Sampaic) of the flow chamber (Slide I⁰¹, Ibidi, Germany) was washed using five chamber volumes (CV) of sulfuric acid (2 M; Merck-Sigma), then five CV of hydrogen peroxide (33%; Merck-Sigma), and rinsed with 10 CV of water,

then 10 CV of PBS. Bovine fibronectin (10 $\mu\text{g}/\text{ml}$ in PBS; Merck-Sigma) was incubated 1 h at room temperature and rinsed with 20 CV of PBS. The chamber was equilibrated with DMEM (Life Technologies) at 37°C, then loaded with P815 cells for 15 min at 37°C. One CV of anti-CD3 (20 $\mu\text{g}/\text{ml}$ final; OKT3 produced by A. Alcover) in DMEM was carefully added, and cells were incubated for 15 min at 37°C. Unbound cells and Abs were cleared by flowing five CV of RPMI 1640 (37°C; Lonza). One CV of human CTLs in RPMI 1640–1% FBS (Lonza) was injected inside the chamber and incubated for 10 min at 37°C. A flow rate of PBS, increasing from 0 to 38.4 ml/min, was applied through the chamber for 115 s using a syringe pump (SP210iW, World Precision Instruments) controlled by a computer and synchronized with image acquisition (three images per s, 1100 \times 840 μm) using an inverted transmission microscope (Axio Observer D1; Zeiss) with a 10 \times /0.3 numerical aperture objective controlled by MicroManager (34).

Image series were analyzed using ImageJ software (32) and the plugin Cell Counter. P815 and CTLs were distinguished by their size, shape, and nucleus/cell ratio. The flow rate value at the cell–cell rupture event was used to compute the dragging force on the released cell according to its size (mean diameter of 8 μm), shape (roughly spherical), and density (mean value 1.20 kg/l). Calibration of dragging force was performed from the sedimentation rate of cells in the chamber (measured PBS density 1.0034 kg/l and dynamic viscosity 0.6998 mPa per s at 37°C) (35) and the theoretical flow speed versus wall distance according to Poiseuille solution to Navier–Stokes formalism for a Reynolds number below 10 characterizing a laminar flow. The number of cells loaded in the chamber and located in the field of view may vary from one experiment to another. Moreover, the CTLs initially retained as conjugates were always lower for Apc-silenced cells, indicating initial adhesion impairment. To give the same weight to each of the four experiments performed on different cell numbers in the overall whisker-boxes, shCtrl ($n = 3745$) and shApc ($n = 1091$) cells released per force interval were scaled to a total number of 250 cells per experiment, 1000 cells after adding the four sets.

Live-cell total internal reflection fluorescence microscopy

Glass-bottom microwell dishes (MatTek) were washed with HCl–ethanol 70%. They were coated with poly-L-lysine 0.002% in water (Sigma-Aldrich) for 30 min at room temperature and then with anti-CD3 (10 $\mu\text{g}/\text{ml}$; UCHT1; BioLegend) overnight at 4°C. Human CTLs were incubated with LysoTracker Deep Red (0.1 μM ; Molecular Probes by Life Technologies) for 45 min at 37°C to label cytotoxic granules. Cells were washed and resuspended in human CD8 medium. A total of 1×10^5 cells were dropped in a microwell, and once cells were seeded, images were acquired in live-cell total internal reflection fluorescence (TIRF) plan every 150 ms for 4 min. TIRF images were acquired with an LSM 780 Elyra PS.1 confocal microscope (Zeiss) using an α Plan Apo 100 \times /1.46 numerical aperture oil immersion objective. Images were analyzed using the TrackMate plugin for ImageJ software (33). A fluorescence threshold above 2 \times the mean granule fluorescence

was set to select strong fluorescence events more likely closer to the plasma membrane.

Cytotoxicity assay

At day 6–8 after initial stimulation, human or mouse CTLs were resuspended in RPMI 1640 plus GlutaMAX-I (Life Technologies) 3% FCS, 10 mM HEPES, and mixed at the indicated ratios with P815 target cells previously coated with anti-human-CD3 (6 µg/ml; UCHT1; BioLegend) or anti-mouse-CD3 (6 µg/ml; 145-2C11; eBioscience) for 45 min at 4°C. Mixed CTLs and target cells were incubated 4 h at 37°C. The percentage of target cell lysis was measured using the CytoTox 96 Non-Radioactive Cytotoxicity Assay (Promega) following manufacturer's instructions. Absorbance at 490 nm was measured using a PR2100 Microplate Reader (Bio-Rad Laboratories).

Degranulation assay

At day 6–8 after initial stimulation, human or mouse CTLs were mixed at a 1:1 ratio with P815 target cells previously coated with the indicated anti-CD3 concentration (for human: OKT3, produced by A. Alcover; for mice: 145-2C11; eBioscience) in presence of anti-CD107a-PE (for human: 1/90, clone H4A3; BioLegend; for mice 2.5 µg/ml, clone 1D4B; BD Biosciences), and incubated for 3 h at 37°C. Alternatively, CTLs were stimulated for the indicated time with coated anti-CD3 (10 µg/ml; clone OKT3 produced by A. Alcover) and soluble anti-CD28 (7 µg/ml; Beckman Coulter). Cells were stained with either anti-human CD8a-allophycocyanin-Cy7 (1/25; BioLegend) or anti-mouse CD8a-PerCP-Cy5.5 (1 µg/ml; BD Biosciences). Events were acquired on a MACSQuant Analyzer (Miltenyi Biotec), and analysis was performed using FlowJo 10 software (FlowJo). All samples were gated on forward and side scatter and for singlets.

Analysis of protein phosphorylation

Mouse T cells were incubated with 20 µg/ml of biotin-conjugated anti-CD3 (145-2C11; eBioscience) and anti-CD28 (eBioscience) Abs for 30 min at 4°C. Cells were washed, resuspend in Opti-MEM plus GlutaMAX-I (Life Technologies), and placed 1 min at 37°C. Streptavidin (10 µg/ml; Sigma-Aldrich) was added, and cells were incubated at 37°C for the indicated times. Ice-cold PBS containing 2 mM orthovanadate and 0.05% sodium azide was added to stop cell stimulation. Cells were lysed in ice-cold lauryl-β-maltoside buffer (20 mM Tris [pH 7.4], 150 mM NaCl, 0.25% lauryl-β-maltoside, 50 mM NaF, 10 mM Na₄P₂O₇, 1 mM EGTA, 2 mM orthovanadate, 1 mM MgCl₂, and protease inhibitor mixture) for 10 min on ice. Cell lysates were cleared by spinning at 20,800 × g for 10 min at 4°C. Equal amounts of protein content measured using the Bio-Rad Protein Assay (Bio-Rad Laboratories) was loaded in NuPAGE 4–12% Bis-Tris gels (Thermo Fisher Scientific). Protein transfer was performed using the Trans-Blot Turbo system (Bio-Rad Laboratories). Membranes were saturated with blocking buffer (Rockland Immunochemicals) and incubated overnight at 4°C or 2 h at room temperature with anti-phospho-Akt (p-Ser473; 1/1000; Cell Signaling Technology), anti-phospho-Erk1/2 (p-Thr202/Tyr204; 1/1000; Cell Signaling Technology), anti-GAPDH (6.6 µg/ml;

Calbiochem). Membranes were then incubated with specific secondary Abs conjugated with Alexa Fluor 680 or DyLight 800 (Thermo Fisher Scientific) for 45 min at room temperature. Near-infrared fluorescence was recorded and quantified using an Odyssey Classic Near-Infrared scanner (LI-COR Biosciences). Band intensity was normalized to control GAPDH. For a pooled analysis of several experiments, normalized intensities were then divided by the mean normalized intensity of the same experiment.

Nuclear NFAT detection

Nuclear NFAT was analyzed by Western blot analysis of cells fractionated for nucleus and cytoplasm separation. Mouse T cells were activated as for analysis of protein phosphorylation, for the indicated times. Cells were lysed in ice-cold low-salt lysis buffer (10 mM KCl, 10 mM HEPES, 0.1 mM EDTA, 0.1 mM EGTA, 1 mM DTT, 50 mM NaF, 10 mM sodium pyrophosphate [Na₄P₂O₇], and a protease inhibitor mixture) for 15 min on ice. Detergent Nonidet P-40 (Sigma-Aldrich) was added (0.45% v/v final), and cells were vortexed for 10 s to break cytoplasmic membranes without altering nuclear membranes. Lysates were centrifuged at 20,800 × g for 30 min at 4°C. Supernatants corresponding to cytosolic fractions were recovered in ice-cold tubes. Pellets containing nuclei were washed once in PBS and resuspended in ice-cold high-salt buffer (20 mM Tris-HCl [pH 8], 1% SDS, 2 mM EDTA, and protease inhibitor mixture), solubilized by sonication (3 × 10 s at 60% power) using a Vibracell 72434 (Bioblock Scientific), then centrifuged at 20,800 × g for 30 min. Supernatants were recovered as nuclear fractions. An equal amount of protein content was measured using the Bio-Rad Protein Assay (Bio-Rad Laboratories) was loaded in NuPAGE 3–8% Tris-Acetate gels (Thermo Fisher Scientific). Protein transfer was performed in a Bio-Rad Mini Trans-Blot system. Membranes were saturated with blocking buffer (Rockland Immunochemicals) and incubated with anti-NFATc2 (NFAT1) (0.25 µg/ml; BD Biosciences), anti-SLP76 (1/1000; Thermo Fisher Scientific) or anti-Lamin B1 (1/2000; Abcam) overnight at 4°C. Then, they were incubated with specific secondary Abs conjugated with Alexa Fluor 680 or DyLight 800 (Thermo Fisher Scientific) for 45 min. Near-infrared fluorescence was imaged and quantified using the Odyssey Classic scanner as described above. NFAT band intensity was normalized to SLP76 cytoplasmic control or Lamin B1 nuclear control. For a pooled analysis of several experiments, normalized intensities were then divided by the mean normalized intensity of the same experiment.

Mouse T cell differentiation and proliferation assays

Mouse cells from 12-wk-old mice freshly isolated from the spleen and lymph nodes were stimulated with concanavalin A (ConA; 5 µg/ml; Sigma-Aldrich) in mouse CD8 medium with IL-2 (10 ng/ml; Miltenyi Biotec) for 2 d and then cultured four additional days with IL-2. At day 0, 2, 4, and 6, cells were incubated with anti-CD16/32 (10 µg/ml; BioLegend) to block Fc receptors and then stained with Fixable Viability Stain 450 (25 ng/ml; BD Biosciences), anti-CD3-FITC (5 µg/ml; 145-2C11, BD Biosciences), anti-CD4-allophycocyanin-Vio770 (1.5 µg/ml; Miltenyi Biotec), anti-CD8-PerCP-Cy5.5 (1 µg/ml; BD Biosciences),

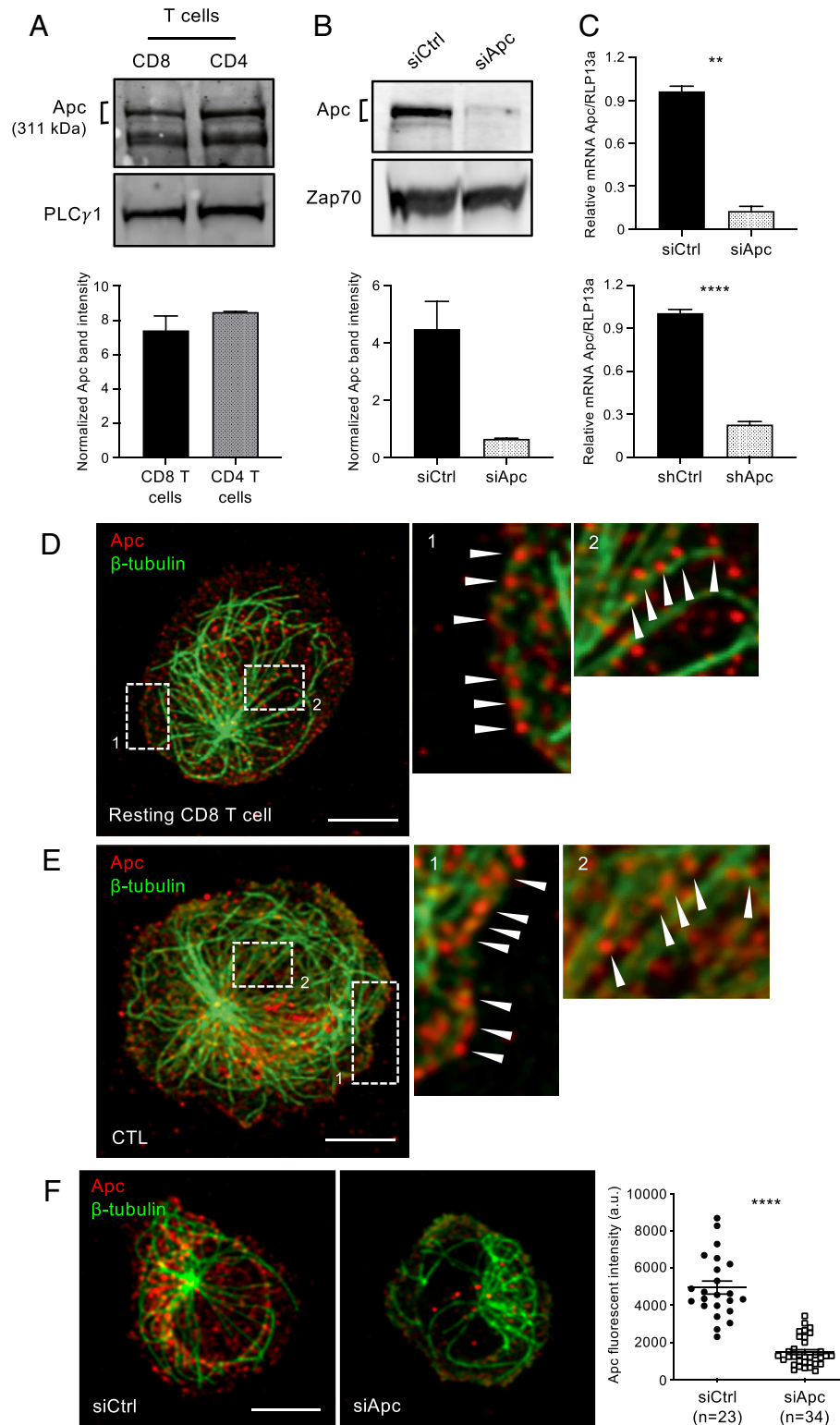


FIGURE 1. Apc is expressed in CD8⁺ T cells.

(A) Expression of Apc in purified primary human CD8 and CD4 T cells. Cell lysates were analyzed by Western blot using anti-Apc and anti-PLC γ 1 Abs. The band corresponding to Apc (~310 kDa) was quantified with respect to the PLC γ 1 band. Data are the mean \pm SEM of three donors. (B) Expression of Apc detected by Western blot in resting primary human CD8 T cells transfected with control or Apc siRNA. Apc band intensity was normalized with respect to ZAP70. Data are the mean \pm SEM of two experiments. (C) Expression of Apc detected by quantitative (Continued)

anti-CD25-PE-Cy7 (2 $\mu\text{g/ml}$; BD Biosciences), anti-granzyme B-A647 (1/50; BioLegend), anti-CD44-allophycocyanin (2 $\mu\text{g/ml}$; eBioscience), and anti-CD62L-RPE (2 $\mu\text{g/ml}$; eBioscience). Events were acquired on a MACSQuant Analyzer (Miltenyi Biotec), and analysis was performed using FlowJo 10 software (FlowJo). All samples were gated on forward and side scatter for singlets, and for live cells, samples were stained using Fixable Viability Stain 450 (250 ng/ml; BD Biosciences).

Proliferation was calculated by counting the cells at day 0, 2, 4, and 6 upon stimulation, as described above for the differentiation assays. Cell numbers were referred to the cell counts at day 0.

Detection of cytokine production

IL-2 was removed from CTL culture, and 20 h later, cytokine production was assessed by ELISA and flow cytometry as follows: for detection by ELISA, 1×3.10^5 human or mouse CTLs were restimulated at 37°C for 6 h with PMA (50 ng/ml; Sigma-Aldrich) and calcium ionophore A23187 (500 ng/ml; Sigma-Aldrich) or 20 h with coated anti-CD3 (for human, 5 $\mu\text{g/ml}$, UCHT1; BioLegend; for mice, 145-2C11, 5 $\mu\text{g/ml}$; eBioscience) and soluble anti-CD28 (for human, 5 $\mu\text{g/ml}$; Beckman Coulter; for mice, 2 $\mu\text{g/ml}$; eBioscience). Secreted IL-2, TNF- α , and IFN- γ levels were measured from culture supernatants with specific DuoSet ELISA Kits (R&D Systems) following manufacturer's instructions.

For detection by flow cytometry, 1×10^5 mouse CTLs were restimulated as described above. Two hours after the beginning of restimulation, brefeldin A (10 $\mu\text{g/ml}$; Sigma-Aldrich) was added. Cells were fixed with 2% paraformaldehyde for 15 min at room temperature, incubated with anti-CD16/32 (10 $\mu\text{g/ml}$; BioLegend), and subsequently stained with anti-IL-2-RPE (4 $\mu\text{g/ml}$; eBioscience), anti-TNF- α -FITC (1.2 $\mu\text{g/ml}$; Miltenyi Biotec) and anti-IFN- γ -PE-Cy7 (8 $\mu\text{g/ml}$; BioLegend) in presence of 0.05% saponin. Events were acquired on a MACSQuant Analyzer (Miltenyi Biotec), and analysis was performed using FlowJo 10 software (FlowJo). All samples were gated on forward and side scatter for singlets, and for live cells, they were stained using Fixable Viability Stain 450 (250 ng/ml; BD Biosciences).

Statistics

Statistical analyses were carried out using Prism Software (GraphPad). Error bars in plots represent the mean \pm SEM. The p values are represented as follows: **** $p < 0.0001$, *** $p < 0.001$, ** $p < 0.01$, * $p < 0.05$, NS $p \geq 0.05$. The type of test used is mentioned in each figure legend.

RESULTS

Apc is expressed in human CD8 T cells

We first investigated the expression of Apc in primary human CD8 T cells. Immunoblotting on cell lysates revealed similar levels in CD4 and CD8 T cells of a protein band consistent with the 311 kDa full-length protein previously described (24, 29) (Fig. 1A). This band disappeared upon siRNA silencing in CD8 T cells (Fig. 1B). Apc depletion was similarly detected by quantitative RT-PCR upon siRNA transfection in human resting CD8 T cells or shRNA retroviral transduction in differentiated CTLs (Fig. 1C). We next analyzed Apc subcellular localization. Both resting and differentiated CD8 T cells showed a punctate pattern of Apc associated with microtubules and aligned at the edges of immunological synapses formed on anti-CD3-coated coverslips (arrowheads) (Fig. 1D, 1E). This Apc pattern was consistent with our findings in CD4 T cells (29) and with previous reports in other cell types (36, 37). The specks pattern was strongly diminished in Apc-silenced T cells (Fig. 1F), further supporting the specificity of the Apc immunofluorescence pattern.

Apc regulates microtubule and actin cytoskeleton remodeling at the immunological synapse

Apc was shown to regulate microtubule network organization in polarized migrating cells (38–40) as well as actin polymerization (41). Furthermore, Apc coordinates actin polymerization and microtubules at focal adhesions in migrating cells (42). In both CD4 and CD8 T cells, actin and microtubule cytoskeletons cooperate to build functional immunological synapses (2, 8, 14). Indeed, in CD8 T cells, microtubule polarization toward target cells combined with actin polymerization, followed by rapid clearance from the center of the synapse, appear to be key for cytolytic granule release and target cell lysis (6, 9, 43). Importantly, we previously showed that Apc silencing in CD4 T cells results in microtubule network disorganization at the immunological synapse (29).

Therefore, we investigated whether Apc controls cytoskeleton remodeling in CD8 T cell immunological synapses. Apc silencing altered microtubule network organization at the immunological pseudosynapses formed by either resting or differentiated CD8 T cells on anti-CD3-coated coverslips. Microtubule patterns were more frequently radially organized in control cells, reaching the synapse periphery and with visible microtubule organizing center. In contrast, Apc-silenced cells more often displayed randomly

RT-PCR in resting primary human CD8 T cells transfected with control or Apc siRNA (top) or ex vivo-differentiated CTLs infected with control or Apc shRNA expressing retroviruses (bottom). Data are the mean \pm SEM of three and five experiments, respectively. Significance was determined by Mann-Whitney U test. (D–F) Resting human CD8 T cells (D and F) or ex vivo-differentiated CTLs (E) were spread on anti-CD3-coated coverslips for 5 min to generate flat immunological pseudosynapses. Cells were then fixed and stained with anti- β -tubulin Ab to reveal microtubules and with anti-Apc Ab. Confocal optical sections were acquired at 0.2- μm intervals. Images were posttreated by deconvolution. A 0.8- μm section at the cell-coverslip contact is shown. Scale bar, 5 μm . (D and E) Right panels are zoomed images of the framed cellular areas corresponding to the periphery of the synapse (D1 and E1) and the center of the cell (D2 and E2). Arrowheads point to Apc puncta. (F) Cells were transfected with control or Apc siRNA. Right panel correspond to the quantification of Apc total fluorescent intensity. Significance was determined by Mann-Whitney U test. ** $p < 0.01$, **** $p < 0.0001$.

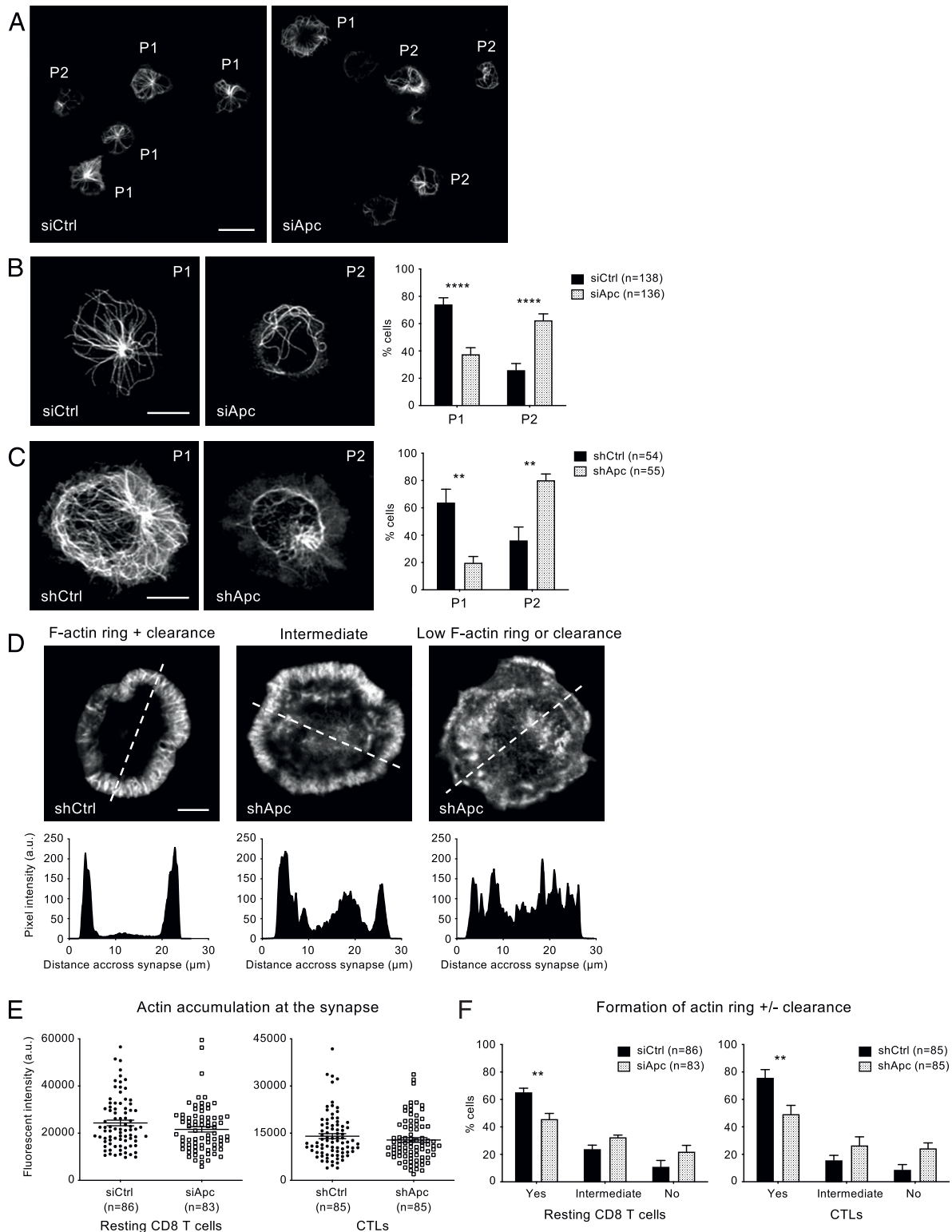


FIGURE 2. Apc controls microtubule and actin cytoskeleton remodeling at the immunological synapse.

(A, B, E left, and F left) Human resting CD8 T cells were transfected with control or Apc siRNA. (C–E right, F right) Human ex vivo–differentiated CTLs were infected with retroviruses expressing control or Apc shRNA and GFP. Cells were stimulated on anti-CD3–coated coverslips for 5 min to generate flat immunological synapses. Cells were then fixed and stained with anti- β -tubulin Ab to label microtubules (A–C) or with phalloidin to label F-actin (D–F). (A–C) Confocal optical sections were acquired at 0.2- μ m intervals. Images were posttreated by deconvolution. **(Continued)**

organized microtubules (Fig. 2A–C). In addition, we observed that actin remodeling at the synapse was also impaired (Fig. 2D–F). Actin could accumulate at the synapse, and no differences between control and Apc-silenced cells were observed with regard to the total amount of F-actin at the contact site (Fig. 2E). However, control cells often formed F-actin rings at the periphery of the synapse, excluding actin from the center (Fig. 2D, left panel, and Fig. 2F). In contrast, Apc-silenced cells less frequently displayed this actin pattern, more often forming synapses with a less defined actin ring and lower clearance from the center (Fig. 2D, center and right panels, and Fig. 2F).

Apc conditions CTL centrosome polarization, immunological synapse shape, symmetry, and stability

Our observations on cytoskeleton remodeling prompted us to investigate a larger number of features of immunological synapses formed between human CTLs and anti-CD3-coated P815 tumor target cells, a model of Ab-mediated T cell cytotoxicity. Following the examples of synapses shown in Fig. 3A, we analyzed the following: 1) CTL centrosome polarization, assessed by the distance of the centrosome (arrows) to the center of the synapse; 2) synapse symmetry, assessed by the relative aligned position of the centrosome and the T cell and target cell nuclei; and 3) synapse shape, assessed by the presence of large membrane extensions (arrowheads). Fig. 3A (left panel) provides an example of a symmetrical CTL–target cell conjugate, with a polarized centrosome (arrow) and no large membrane extensions. The right panel is an example of an asymmetrical conjugate, with the centrosome poorly polarized and displaying large cell extensions (arrowheads) and a more irregular shape. We observed that Apc silencing did not alter the number of conjugates (data not shown) but impaired T cell centrosome polarization toward the synapse and T cell symmetry and increased the presence of large cell extensions (Fig. 3B–D). These features may reflect or be the cause of the inability of Apc-silenced cells to make stable interactions with target cells.

To obtain further insight into the effect of Apc silencing on the stability of CTL–target cell conjugates, we measured the rupture force of cell–cell interactions between CTLs and anti-CD3-coated P815 cells immobilized in a microscope laminar flow chamber undergoing increasing flow rate. A laminar shear flow rate was applied, generating dragging forces from 0 to 5 nN on individual

cells with an increasing slope of 34 pN/s. CTLs interacting with immobilized P815 were stretched by this dragging force until rupture of the contact and release of the T cells into the stream (Fig. 3E; Supplemental Video 1). CTL–P815 cell rupture forces ranged from 0 to 4.5 nN, with half of the values between 0.5 and 2.5 nN, suggesting a large variety of synapse formation kinetics or complexity. Median rupture forces were 1.52 and 0.67 nN for control and Apc-silenced cells, respectively, indicating that the interacting force was decreased by loss of Apc expression (Fig. 3F). Interestingly, cumulative plots of cell–cell rupture events versus dragging force show linear distributions for control cells and hyperbolic distributions for Apc-silenced cells (Fig. 3G). Of note is that, although equal cellular input of shCtrl and shApc cells was applied to the chamber, the number of CTLs forming initial conjugates with P815 cells before applying flow pressure was lower in shApc-treated cells in most experiments (n in Fig. 3F legend). This further reflects the lower capacity of Apc-silenced cells to initially stabilize conjugates with P815 target cells. To give the same weight to each of the four experiments performed on different cell numbers in the combined data whisker-boxes, shCtrl ($n = 3745$) and shApc ($n = 1091$) cells released per force interval were scaled to a total number of 250 cells per experiment, 1000 cells after adding the four sets.

Therefore, Apc silencing affects centrosome polarization, immunological synapse shape and symmetry, and the stability of CTL–tumor target cell interactions.

Apc controls lytic granule dynamics, targeting, and fusion at the immunological synapse

Perturbation of actin and microtubule remodeling at the immunological synapse, T cell centrosome polarization, and the stability of CTL–target cell interactions of Apc-silenced cells (Figs. 2, 3) might result in reduced accessibility of lytic granules to the immunological synapse, reducing the capacity of CTLs to kill target cells (6, 7, 9).

To investigate this, we first analyzed lytic granule dynamics at the immunological synapse. Human control or Apc-silenced CTLs were labeled with LysoTracker and set on anti-CD3-coated coverslips to obtain flat immunological synapses. Granule dynamics were then followed by live-cell TIRF microscopy. We measured the following events occurring at the TIRF plan during

A 0.8- μm section at the cell–coverslip contact is shown. Microtubule network organization patterns at the immunological synapse were ranked by observation of unlabeled images by three independent investigators in two categories: pattern 1 (P1), presence of a radial plane of microtubules, or pattern 2 (P2), nonradial organization. Data are the mean \pm SEM of three siRNA experiments and two shRNA experiments in duplicates. Significance was determined by two-way ANOVA. Scale bar, 10 μm (A) and 5 μm (B and C). (D–F) Confocal optical sections were acquired at 1- μm intervals; a section at the cell–coverslip contact is shown. F-actin organization patterns at the immunological synapse were ranked in three categories depending on the pixel intensity plot across the synapse (lower panels): F-actin ring plus clearance, centrally depleted actin, and accumulation at the periphery of the synapse; intermediate, uneven depletion of F-actin at the center of the synapse; low F-actin ring or clearance, F-actin all across the synapse. Analyses were performed on a 1- μm section at the cell–coverslip contact. Data are the mean \pm SEM of two siRNA experiments and three shRNA experiments in duplicates. Significance was determined by two-way ANOVA. Scale bar, 5 μm . (E and F) Quantification of total F-actin (E) and F-actin phenotype (F) at the immunological synapse in human resting CD8 T cells transfected with siCtrl or siApc (left panels) or in human CTLs expressing shCtrl or shApc (right panels). ** $p < 0.01$, **** $p < 0.0001$.

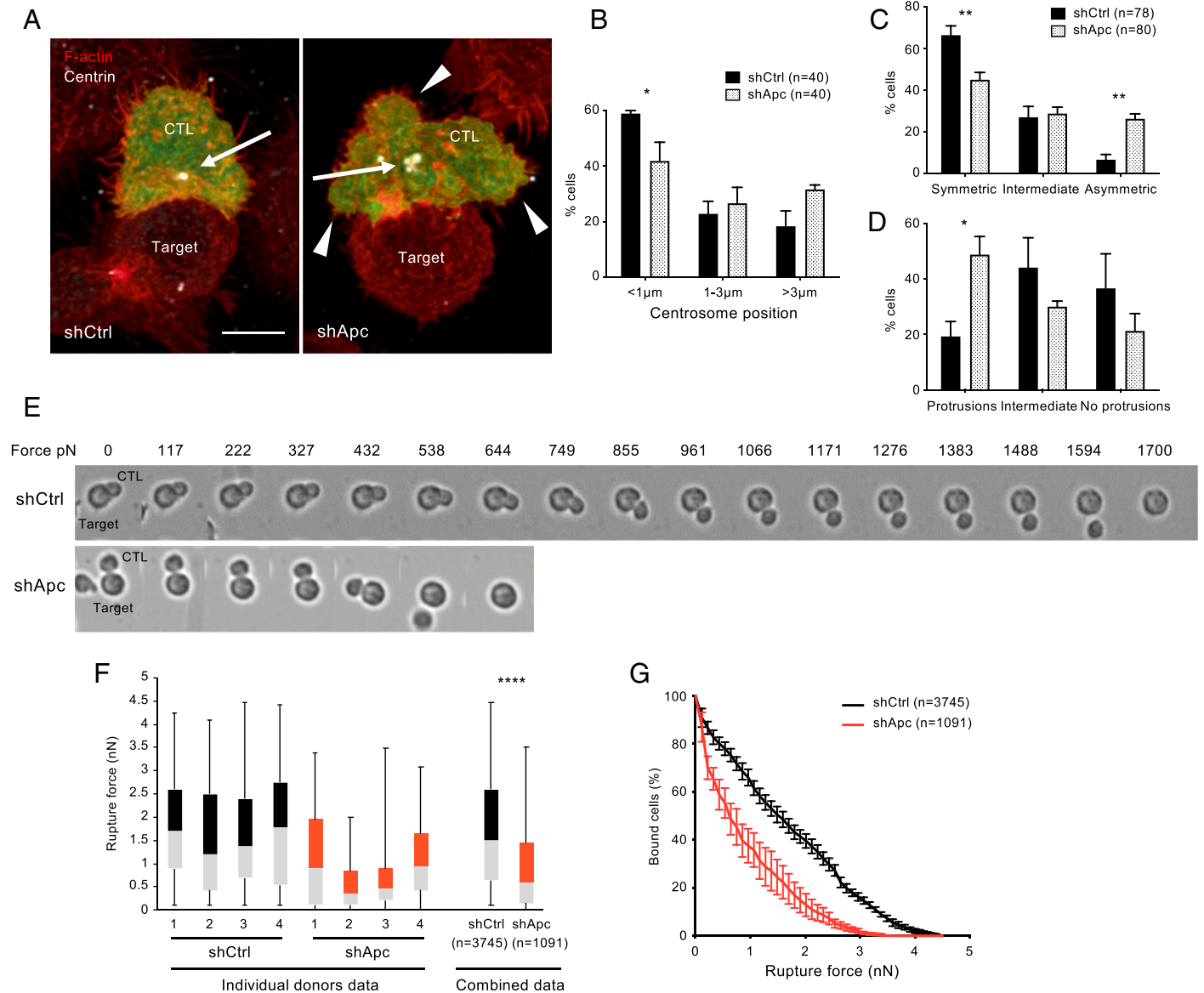


FIGURE 3. Apc controls centrosome polarization and immunological synapse shape, symmetry, and stability.

(A) Control or Apc-silenced human ex vivo-differentiated CTLs were incubated with anti-CD3-coated P815 for 15 min. Cells were then fixed and stained with phalloidin (red) to label F-actin and anti-pericentrin Ab to label the centrosome (white, arrows). Control and Apc shRNA-infected cells are GFP⁺ (green). Confocal optical sections were acquired at 0.2- μm intervals. Images were posttreated by deconvolution. Conjugate 3D reconstructions are shown. Arrows point to centrosomes, and arrowheads point to membrane extensions. Scale bar, 5 μm . (B) Centrosome distance relative to the synapse. Data are the mean \pm SEM of two experiments in duplicates. Significance was determined by unpaired *t* test. (C and D) Morphological analysis of the synapses. Cell symmetry (C) and the presence of protrusions (A, arrowhead, and D) were analyzed by observation of unlabeled images by three independent investigators. Data are the mean \pm SEM of four experiments in duplicates. Significance was determined by unpaired *t* test. (E–G) Control or Apc-silenced human CTLs were set to interact with anti-CD3-coated P815 tumor target cells previously adhered to a fibronectin-coated laminar flow chamber for 10 min at 37°C. Then, a laminar flow of PBS increasing from 0 to 38.4 ml/min was applied through the chamber for 115 s using a computer-driven syringe pump and synchronized with image acquisition (three images per s). (E) Representative images of Supplemental Video 1, showing the sequential steps of CTL detachment from the target cell. CTLs are distinguished from target cells by their larger size, cytoplasm, and light refringency. Top line, shCtrl (original magnification $\times 250$), and bottom line, shApc-treated cells (original magnification $\times 300$). Force in nN corresponding to each image is depicted. (F and G) Quantification of rupture forces of interactions between CTLs and anti-CD3-coated P815 cells. Force was calculated as described in *Materials and Methods*. (F) Four healthy donors (1–4) treated with shCtrl ($n = 684, 671, 1189, 1201$) or with shApc ($n = 576, 239, 124, 152$) were analyzed. Whiskers represent minimum and maximum values, whereas gray and black or red boxes represent second and third quartile framing the median. Plots on the right show the combined data from the four donors. Significance determined by Mann–Whitney *U* test. (G) Cumulative plots of cell–cell rupture events versus dragging force combining data from the four donors. For each point, mean \pm SEM are shown. * $p < 0.05$, ** $p < 0.01$, **** $p < 0.0001$.

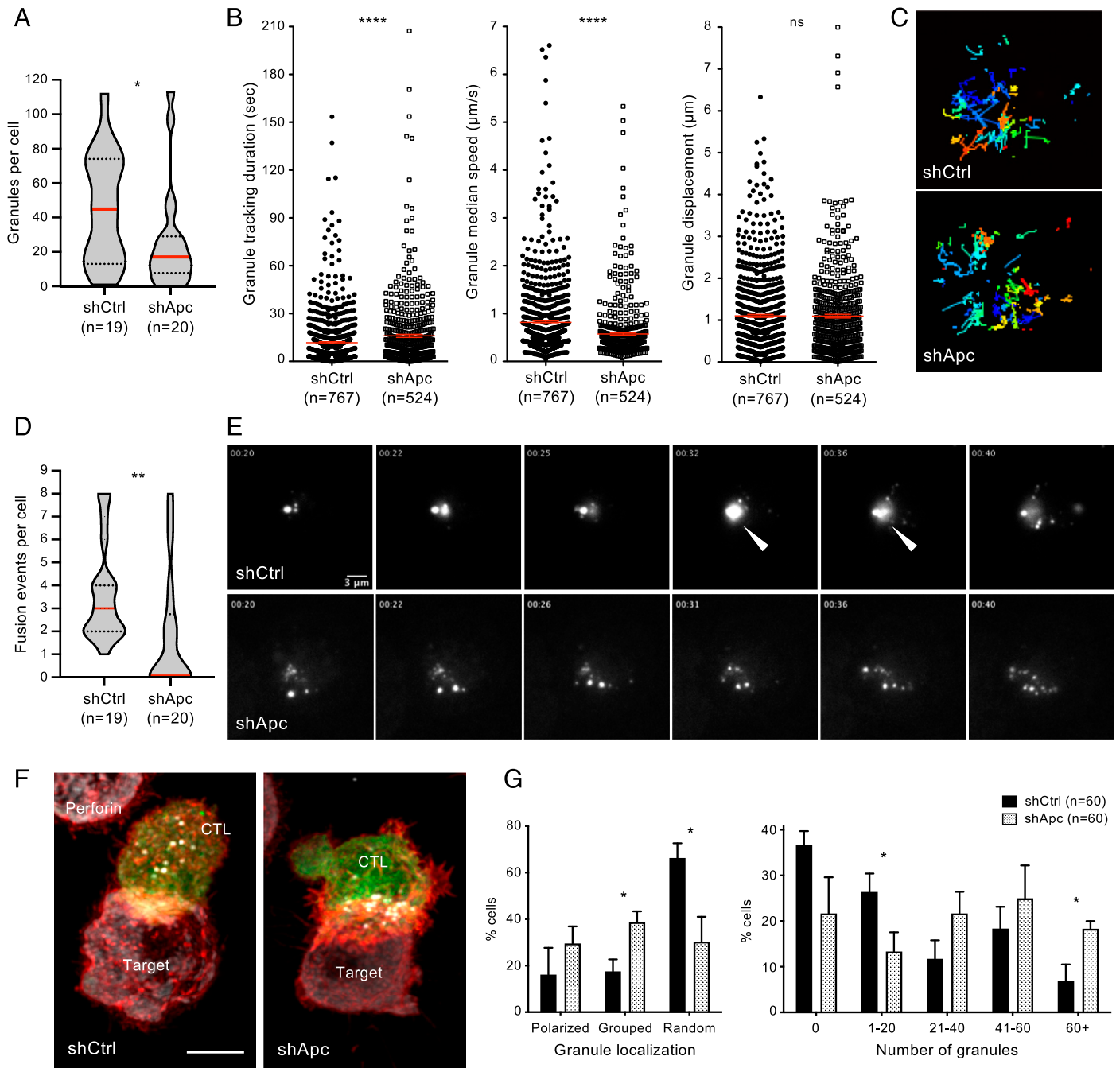


FIGURE 4. Apc controls lytic granule dynamics, targeting, and fusion at the immunological synapse.

(A–E) Control or Apc-silenced human ex vivo–differentiated CTLs were incubated with LysoTracker to label lytic granules as part of the late endosomal-lysosomal compartment. Cells were then set on anti-CD3–coated coverslips to generate flat immunological synapses. LysoTracker⁺ granules were tracked using live-cell TIRF microscopy, which allows the observer to follow vesicles within 200-nm distance from the immunological synapse plasma membrane and therefore detects lytic granule targeting and fusion events (fluorescence burst, arrowhead), as well as granule dynamics at immunological synapse. TIRF images were acquired every 150 ms during 4 min. Quantitative data are the mean ± SEM of three experiments. (A) The number of lytic granules detected per synapse was used as a readout of granule–targeting events (see also Supplemental Video 2). (B and C) Granule dynamics were estimated by tracking individual granules (C). Scale bar, 3 µm. Tracking duration, average speed, and displacement length were assessed (B). (D and E) Among the detected lytic granules, some made a fluorescence burst, indicative of fusion with the plasma membrane. The number of bursts was used as a readout of granule fusion events. (see also Supplemental Video 2). (F) Control or Apc-silenced human ex vivo–differentiated CTLs were incubated with anti-CD3–coated P815 for 15 min. Cells were then fixed and stained with phalloidin (red) and anti-perforin (white) to label cytotoxic granules. Control and Apc shRNA-infected cells are GFP⁺. Confocal (Continued)

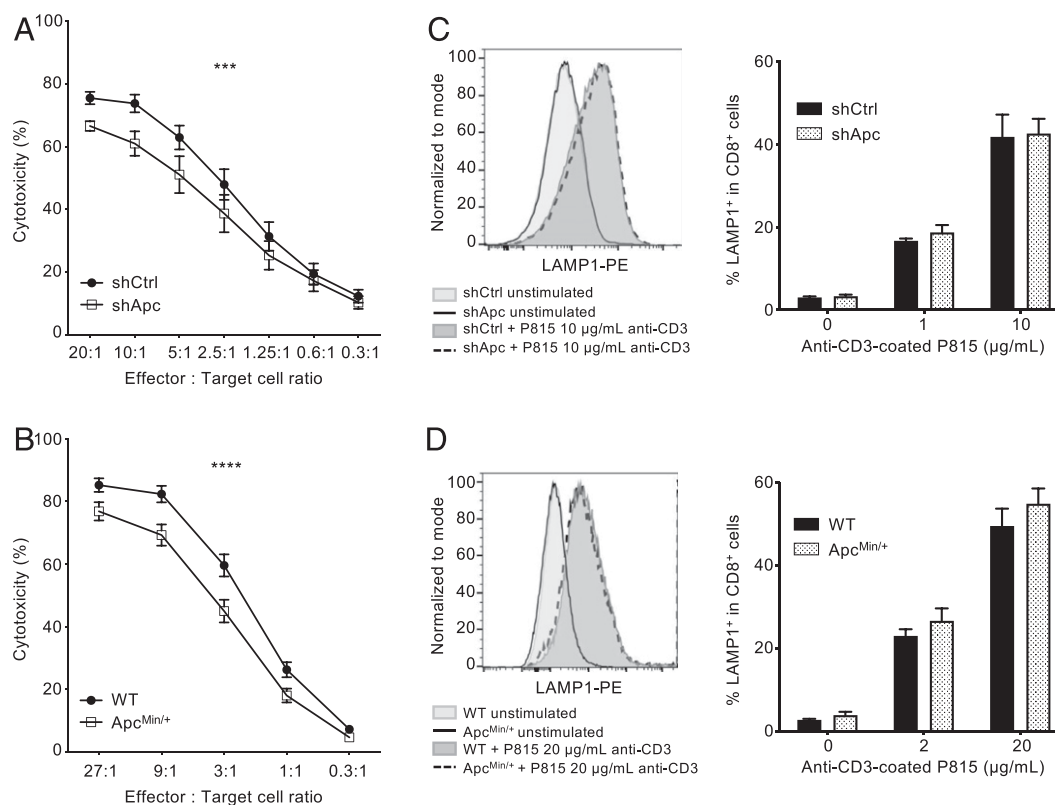


FIGURE 5. Apc controls CTL killing of tumor target cells.

(A and B) Control or Apc-silenced human ex vivo-differentiated CTLs (A) or ex vivo-differentiated CTLs from wild-type or Apc^{Min/+} mice (B) were mixed with anti-human or mouse CD3-coated P815 tumor target cells at the depicted effector CTL/target cell ratios and incubated for 4 h. Killing was assessed by a colorimetric assay as described in *Materials and Methods*. Data are the mean \pm SEM of six shRNA experiments and 12 mice in duplicates. Significance was determined by two-way ANOVA. (C and D) Human (C), or mouse (D) CTLs obtained as in (A) and (B) were incubated with P815 tumor target cells coated with anti-human or anti-mouse CD3 at the depicted concentration. Anti-LAMP1-PE (CD107a) was added to the cells and incubated for 3 h. LAMP1 expression was analyzed by flow cytometry. Representative FACS plots are displayed in left panels and the percentage of cells overexpressing LAMP1 upon target cell incubation is shown in right panels. Data are mean \pm SEM of four shRNA experiments and six mice in duplicates. *** $p < 0.001$, **** $p < 0.0001$.

4 min recording: 1) the total number of bright fluorescence spots as a readout of granules targeted to the synapse; 2) the granule movement by tracking individual fluorescent particles at the synapse; and 3) the number of granules generating a fluorescence burst as a readout of granule fusion with the plasma membrane (6, 9). Representative images are shown in Fig. 4E and Supplemental Video 2. Quantification showed that Apc-silenced cells displayed reduced targeting events (Fig. 4A). Furthermore, lytic granules in Apc-silenced cells remained for longer times at the synapse, and their speed was lower than in control cells (Fig. 4B). However, the length of displacement of granules was similar in control and Apc-

silenced CTLs (Fig. 4B, 4C). Importantly, Apc-silenced cells displayed fewer fusion events (Fig. 4D, 4E, arrowheads, and Supplemental Video 2). Therefore, loss of Apc expression alters lytic granule dynamics, targeting, and fusion at the immunological synapse.

We next studied immunological synapses formed between CTLs and anti-CD3-coated P815 tumor cells upon 15 min of CTL-target cell contact. Subcellular localization of lytic granules was assessed by anti-perforin Ab staining. Interestingly, control cells displayed a low number of randomly distributed lytic granules (Fig. 4F, left panel, and Fig. 4G), whereas Apc-silenced cells

optical sections were acquired at 0.2- μ m intervals. Images were posttreated by deconvolution. Conjugate 3D reconstructions are shown. Scale bar, 5 μ m. (G) Lytic granule localization and quantification. Cells were ranked in three categories depending on granule patterns by blinded image analyses of three independent investigators. Polarized: granules are grouped and localized close to the immunological synapse; grouped: granules are grouped but far from the synapse; random: granules are randomly distributed throughout the cell. The total number of lytic granules was quantified using the TrackMate plugin on ImageJ. Data are mean \pm SEM of three experiments in duplicates. Significance was determined by unpaired *t* test. * $p < 0.05$, ** $p < 0.01$, **** $p < 0.0001$, ns ≥ 0.05 .

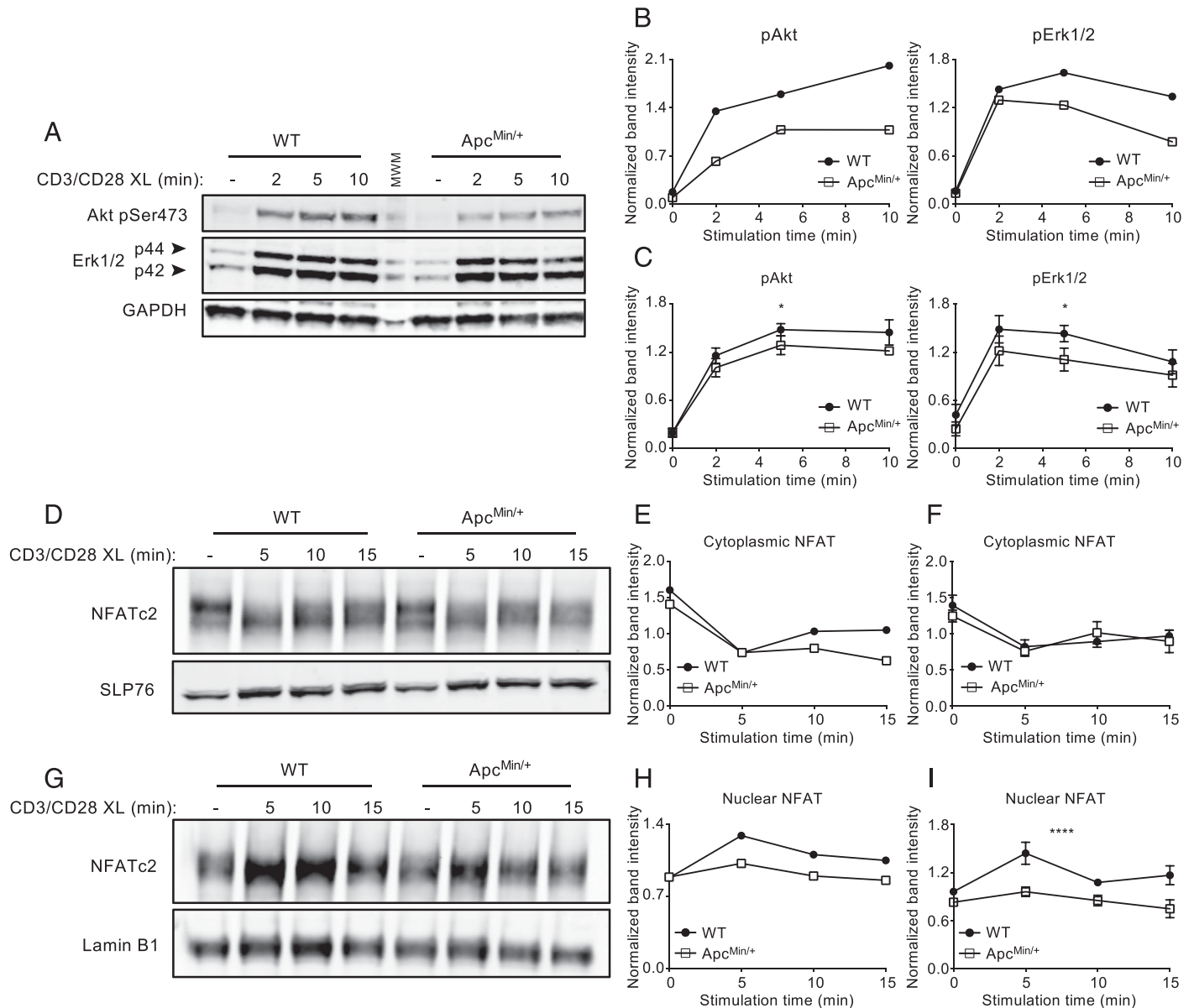


FIGURE 6. *Apc* modulates early T cell activation and NFAT nuclear translocation.

Ex vivo-differentiated CTLs from wild-type or *Apc^{Min/+}* mutant mice were stimulated with anti-CD3 and anti-CD28 Abs for the indicated times. Cells were subsequently lysed, and the depicted signaling proteins were analyzed by immunoblotting. (A–C) Quantification of Akt and Erk1/2 phosphorylation following CTLs stimulation. pAkt and pErk1/2 band intensities were normalized with respect to GAPDH used as loading control. Normalized intensities were then divided by the mean normalized intensity of the same experiment before pooling data from multiple experiments. Data are representative of one experiment (B) or are mean \pm SEM of seven mice (C). Significance was determined by two-way ANOVA. (D–I) Quantification of NFAT nuclear translocation following CTLs stimulation. Cell lysates were lysed, separated into cytoplasmic (D) and nuclear (G) fractions, and analyzed by immunoblotting. NFAT band intensity was normalized with respect to SLP76 or lamin B1, used as loading control, then divided by the mean normalized intensity of the same experiment to normalize between different experiments. Data are representative of one experiment (E and H) or are mean \pm SEM of three mice (F and I). Significance was determined by two-way ANOVA. * $p < 0.05$, **** $p < 0.0001$.

displayed a higher number of granules that were more grouped and polarized toward the synapse (Fig. 4F, right panel, and Fig. 4G).

These data suggest that in *Apc*-silenced cells lytic granules can group close to the centrosome and reorient toward the synapse;

however, they are less efficiently targeted and fused to the synapse plasma membrane. As a consequence, a higher number of lytic granules is retained in CTLs during their interaction with target cells.

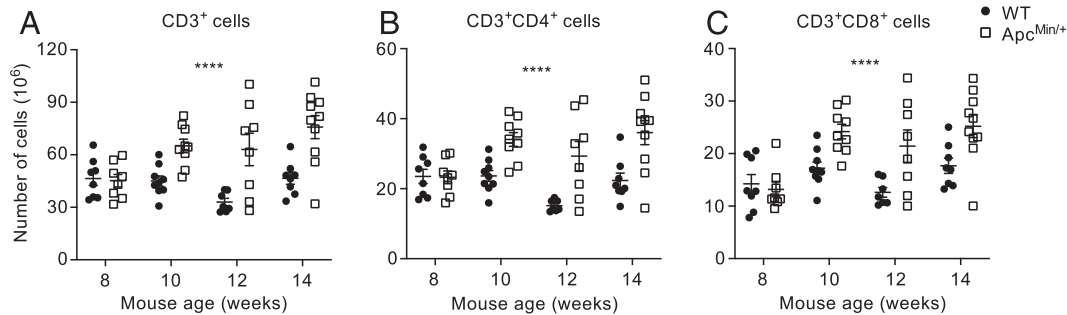


FIGURE 7. *Apc*^{Min/+} mice do not have defects in T cell numbers in vivo.

Cells from wild-type and *Apc*^{Min/+} mice at 8, 10, 12, or 14 weeks of age were extracted from spleen and lymph nodes and counted. Numbers of CD3⁺ (A), CD3⁺CD4⁺ (B), and CD3⁺CD8⁺ (C) were calculated after flow cytometry analyses of cells stained with anti-CD3, anti-CD4, and anti-CD8 Abs. Each dot represents a mouse. Horizontal bars are the mean \pm SEM. Significance was determined by two-way ANOVA. *****p* < 0.0001.

Apc regulates CTL killing of tumor target cells

We next asked whether the defects in cytotoxic granule dynamics observed in *Apc*-silenced cells could impair their capacity to kill tumor target cells. To this end, we used conventional longer incubation assays to measure degranulation and tumor target cell killing. Both human *Apc*-silenced CTLs and mouse *Apc*^{Min/+} CTLs were less efficient in killing anti-CD3-coated P815 tumor target cells, as assessed by a lactate dehydrogenase–release colorimetric assay (Fig. 5A, 5B). However, no significant differences were observed in the capacity of these human and mouse CTLs to degranulate, as assessed by measuring cell surface expression of the LAMP1 luminal epitope CD107a upon CTL contact with anti-CD3-coated P815 tumor target cells for 3 h (44) (Fig. 5C, 5D).

To investigate the apparent contradiction between a less efficient lytic granule fusion at the immunological synapse of *Apc*-silenced cells and no alteration in LAMP1 expression, we stimulated the cells under the same conditions used for granule fusion detection, and we shortened the kinetics. No significant changes in LAMP1 expression between control and *Apc*-silenced CTLs were observed under these experimental conditions either (Supplemental Fig. 1). This dichotomy has been reported by others (45) and may account for LAMP1⁺ vesicle release in an unpolarized manner in response to calcium signals despite a less efficient lytic granule delivery at the CTL–target cell interface and reduced killing.

Altogether, the above described data indicate that *Apc* is necessary for efficient microtubule and actin cytoskeleton remodeling conditioning, lytic granule targeting and fusion at the immunological synapse, and ultimately, efficient killing of tumor target cells.

Apc modulates T cell signaling and NFAT nuclear translocation

We had shown in CD4 T cells that the polarity regulators Dlg1 and *Apc* were involved in microtubule network organization at the immunological synapse, conditioning NFAT transcriptional activation (14, 29, 46). We therefore investigated whether *Apc* modulation of cytoskeleton remodeling could affect CD8 T cell activation. To this end, we analyzed the capacity of ex vivo-differentiated CTLs from control and *Apc*^{Min/+} mutant mice to

respond to anti-CD3 plus anti-CD28 stimulation. *Apc*^{Min/+} CTLs exhibited a mild but significantly reduced capacity to activate Erk and Akt serine-threonine kinases as assessed by the phosphorylation of regulatory residues of these kinases (Fig. 6A–C). In contrast, the upstream protein tyrosine kinase ZAP70 was more variably activated, and no significant differences between control and *Apc*^{Min/+} cells could be appreciated (data not shown).

Furthermore, NFATc2 nuclear translocation in response to anti-CD3 plus anti-CD28 stimulation was reduced in *Apc*^{Min/+} CTLs (Fig. 6D–I).

Apc defects mildly alter ex vivo differentiation of CD8 T cells

We then investigated whether *Apc* mutation was leading to defects in long-term T cell survival affecting T cell numbers in vivo. To this end, T cells from the spleen and lymph nodes were phenotyped and counted just upon the mice's euthanasia. *Apc*^{Min/+} mice did not show evident defects because they presented similar T cell numbers at 8 wk of age and even higher T cell numbers at 10, 12, and 14 wk of age (Fig. 7). This T cell number increase coincided with the increasing development of intestinal adenomatous polyps in *Apc*^{Min/+} mice.

Next, we analyzed whether *Apc* defects could be associated with impaired CD8 T cell proliferation and differentiation upon in vitro T cell stimulation. Splenocytes and lymph node cells were stimulated with ConA and IL-2, and the proliferation and expression of the activation/differentiation molecules CD25, granzyme B, CD44, and CD62L was assessed at 2, 4, and 6 d upon activation. Expression of CD44 and CD62L adhesion molecules in CD8 T cells from *Apc*^{Min/+} mice appeared mildly affected, mainly at day 2, and granzyme B was affected at day 6. CD62L and granzyme B expression tended to be lower, but the high variability among the animals made differences between wild-type and *Apc*^{Min/+} statistically NS (Fig. 8A–D, 8G, 8H). In contrast, no differences were observed in CD25 expression (Fig. 8E, 8F). Interestingly, differences in CD44 and CD62L expression were more readily observed in CD4 T cells, with more pronounced and longer effects, and the level and kinetics of CD62L expression in CD4 T cells were different from in CD8 T cells (Supplemental

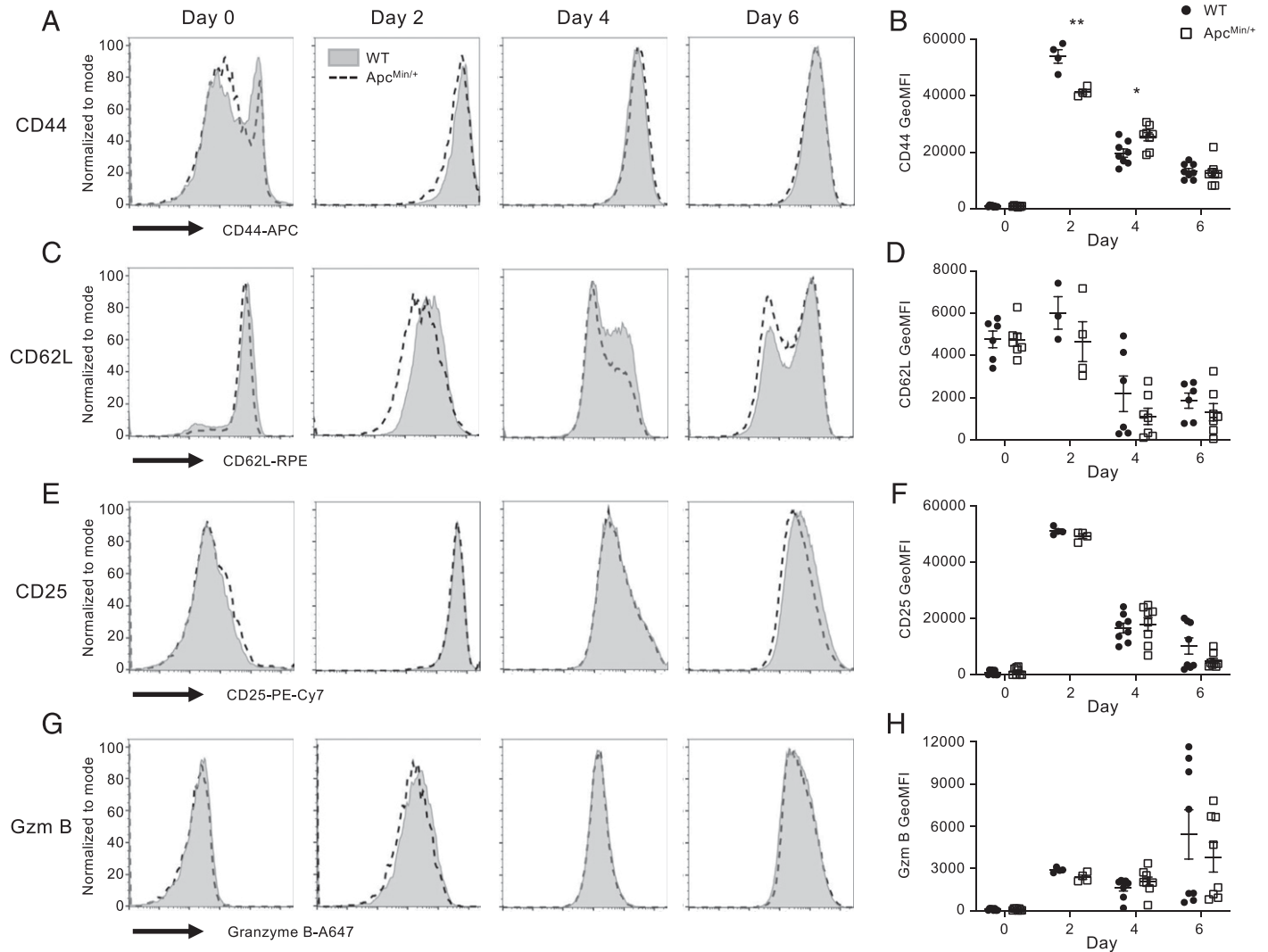


FIGURE 8. *Apc* defects mildly affect CD8 T cell differentiation ex vivo.

Wild-type and *Apc*^{Min/+} mouse cells from spleen and lymph nodes were stimulated for 2 days with ConA, then cultured in the presence of IL-2. CD8 T cell differentiation was assessed at the depicted day after stimulation, quantifying by flow cytometry the expression of the following activation-differentiation markers: CD44, CD62L, CD25, and granzyme B (GzmB). (A, C, E, and G) Flow cytometry profiles of a representative experiment showing CD44, CD62L, and CD25 cell surface expression and intracellular granzyme B, gating on CD3⁺CD8⁺ population. (B, D, F, and H) Quantification of the expression of CD44, CD62L, CD25, and granzyme B at the indicated days. Each dot corresponds to one mouse (mean ± SEM; significance was determined by unpaired *t* test). **p* < 0.05, ***p* < 0.01.

Fig. 2A–F). However, no significant differences in the proliferative capacity were found within the same experimental setting (Supplemental Fig. 2G–I).

These findings show that CD8 T cells from *Apc*^{Min/+} mice present mildly reduced early T cell activation events, such as Erk and Akt activation, and NFAT nuclear translocation as well as mild changes in CD44, CD62L, and granzyme proteins expressed during differentiation ex vivo.

***Apc* defects do not alter ex vivo CTL cytokine production**

Because NFAT drives the transcription of a variety of T cell cytokines, we investigated the capacity of *Apc*-silenced human

CTLs and *Apc*^{Min/+} CTLs to produce effector cytokines. Despite the reduced capacity of *Apc*^{Min/+} CTLs to induce NFAT nuclear translocation, we did not observe significant differences in the production of IL-2, IFN- γ , or TNF- α by differentiated CTLs restimulated with anti-CD3 plus anti-CD28, either by intracellular staining and FACS analysis or by ELISA of cell culture supernatants (Fig. 9A, 9B). Similar results were found when assessing cytokine production in cell culture supernatants of control and *Apc*-silenced human CTLs by ELISA (Fig. 9C).

These findings indicate that *Apc* defects in both human and mouse CTLs do not affect their capacity to produce effector CD8 cytokines under our ex vivo stimulation conditions.

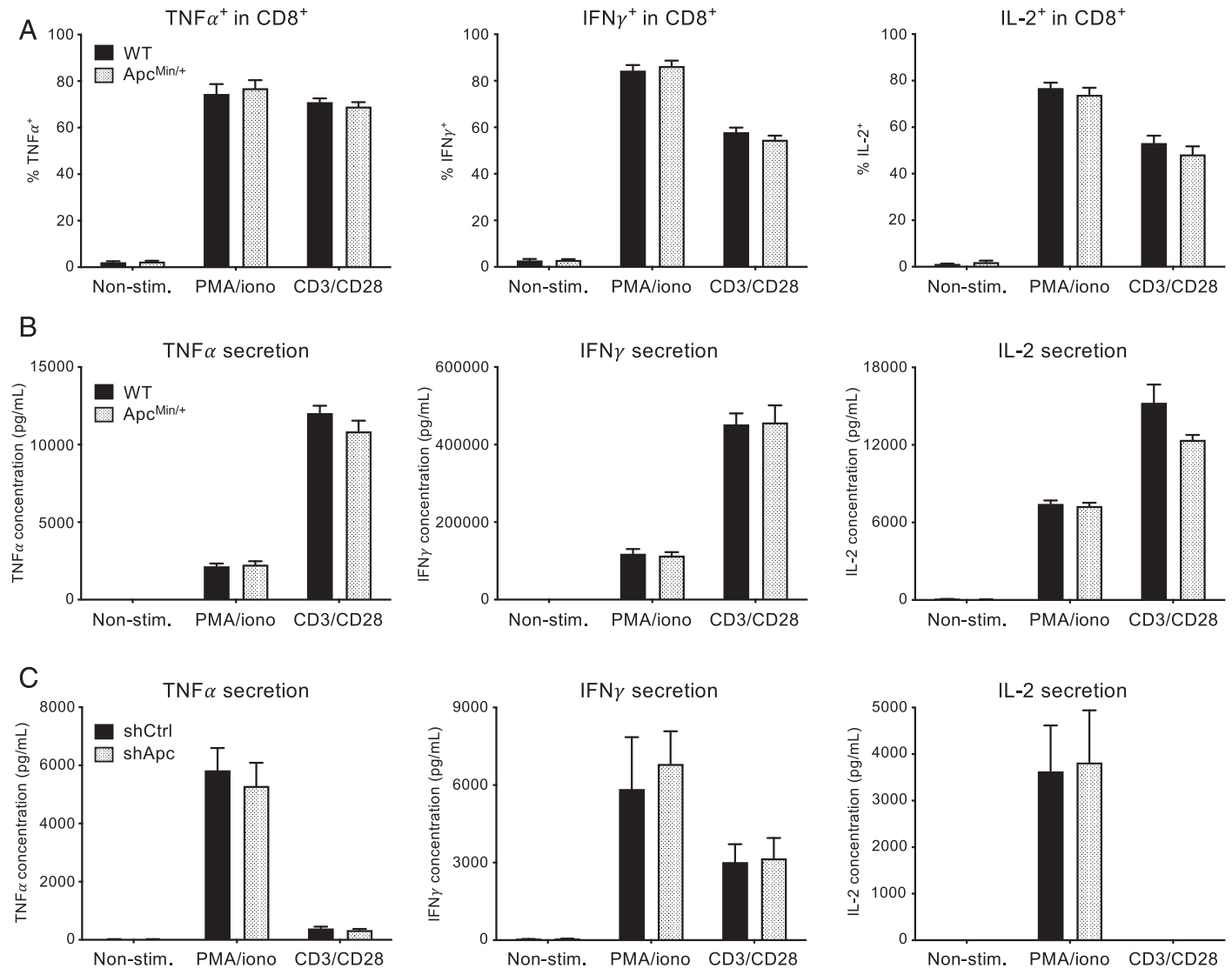


FIGURE 9. Apc defects do not alter CTL cytokine production.

(A and B) Ex vivo-differentiated CTLs from wild-type or Apc^{Min/+} mice were stimulated with anti-CD3 and anti-CD28 Abs for 20 h or PMA and ionomycin for 6 h. The production of TNF- α , IFN- γ , and IL-2 was analyzed by intracellular staining and FACS (A) or ELISA (B). Percentage of cytokine-positive cells was quantified by FACS. Data are mean \pm SEM of 12 mice (A). Cytokine secretion was assessed by ELISA. One representative experiment with four mice is shown out of three experiments (B). (C) Control or Apc-silenced human ex vivo-differentiated CTLs were stimulated with anti-CD3 and anti-CD28 Abs for 20 h or PMA and ionomycin for 6 h. Cytokine production was detected by ELISA. Data are mean \pm SEM of three experiments.

DISCUSSION

Altogether, the data shown in this study unveil a novel role of Apc in cytotoxic T cell effector functions. Apc-silenced human peripheral blood CD8 T cells allowed us to reveal the importance of Apc in cytoskeleton remodeling at the immunological synapse. Both microtubules and actin reorganization appeared affected. Thus, the radial organization of microtubules and centrosome polarization were perturbed, and F-actin ring formation at the periphery of the synapse and F-actin exclusion from the center of the synapse were impaired in Apc-defective T cells. Additionally,

consistent with an impact on actin cytoskeleton dynamics (47), synapse stability, shape, and symmetry were also altered in Apc-deficient cells.

Apc regulation of microtubule organization in CD8 T cells is consistent with the described role of Apc as a polarity regulator in other cell systems (23). Apc performs this function in association with other regulators of cell polarity, including Cdc42, Scribble, Par6, PKC ζ , and Dlg1, as shown, for instance, in migrating astrocytes (40, 48). Furthermore, we have shown before that Dlg1 and Apc control microtubule patterns, centrosome polarization, and signaling microcluster dynamics at the immunological synapse

of CD4 T cells (14, 29). Although less extensively studied, Apc may also regulate actin polymerization in synergy with its partner, the formin family protein mDia (41). In addition, Apc regulates actin-microtubule cross-talk at focal adhesions of migrating cells (42). Interestingly, molecular partners of Apc, such as Cdc42 (40) and formins (41), were shown to control actin remodeling and centrosome polarization at the immunological synapse (49, 50). Therefore, Apc may collaborate with these cytoskeleton regulators to collectively reorganize both cytoskeleton components at the CTL immunological synapse, thus ensuring their interplay, which is crucial for properly tuning T cell functions.

Concomitant centrosome polarization and F-actin exclusion from the center of the immunological synapse has been shown to be key for lytic granule targeting and fusion at the synapse and efficient cytotoxic function against infected or tumor target cells (6, 7, 9, 43). Therefore, impairment of both microtubule organization and centrosome polarization, together with F-actin reorganization at the synapse in Apc-defective CTLs, may account for their altered lytic granule dynamics, targeting, and fusion at the synapse observed by live-cell TIRF microscopy. Apc-silenced cells could still concentrate lytic granules in the centrosomal area and polarize them to a certain extent toward the immunological synapse, suggesting that there is not a complete failure in granule transport on microtubules. Granules may be able to move toward the centrosome and microtubules minus end, a movement mediated by dynein motors. In contrast, granules do not properly reach the immunological synapse plasma membrane. Disorganization of microtubule network at the immunological synapse likely prevents microtubules from reaching the plasma membrane and, as a consequence, precludes centrosome closing up to the synapse, which facilitates lytic granule docking and fusion (7). Kinesin-mediated transport to the microtubules plus end may also help granules to reach the synapse plasma membrane (51, 52). As a likely consequence of inefficient lytic granule dynamics, targeting, and fusion, Apc-defective CTLs killed tumor target cells less efficiently than control cells. However, no difference in degranulation as assessed by increase in LAMP1 (CD107a) cell surface expression was detected. The apparent contradiction between the live-cell TIRF experiments and LAMP1 expression may be due to the distinct sensitivities of the two assays to discriminate differences. In particular, the fact that the LAMP1 vesicular compartment is larger than the lytic granule compartment and may fuse in a nonpolarized manner in response to normal calcium influx in Apc-silenced cells (29) could explain this dichotomy of findings. Of note, lack of direct correlation between degranulation and cytotoxicity has been reported in other experimental setups (45, 53).

Interestingly, our findings share a number of features with those previously reported in CTLs from Wiscott–Aldrich Syndrome patients, who carry mutations in the gene encoding the WAS protein (WASP), a key regulator of actin cytoskeleton dynamics. Thus, in vitro-derived CTLs from WAS patients had a lower capacity to kill tumor target cells, whereas they display equivalent degranulation as assessed by LAMP1 expression. Furthermore, although WAS CTLs could reorient their centrosome

and lytic granules to the target cells, lytic granule distance to the immune synapse was higher than that of healthy donor cells. Finally, WAS CTLs displayed impaired synaptic ring formation, distorted less symmetric CTL–target cell synapses with lower stability, and delayed lethal hit (45, 54). However, WAS CTLs displayed defects in cytokine production, contrary to the Apc-defective CTLs described in this study (45).

Although significant, the differences in tumor cell killing activity between Apc-defective CTLs and control cells were modest. This may be due to the fact that *Apc^{Min/+}* mice are heterozygous (homozygous mutation is embryonically lethal) (55) and may express residual levels of Apc protein. Likewise, shRNA silencing in human primary CTLs is not fully efficient. Hence, remaining Apc protein could account for the observed function. Furthermore, other polarity regulators acting together with Apc may also compensate Apc defects. Finally, the T cell activation conditions we used for CTL generation in vitro may compensate, in part, for cytotoxicity defects because of Apc by increasing the expression of other proteins. This effect was described for some forms of familial hemophagocytic lymphohistiocytosis because of syntaxin 11 or Munc 18-2 mutations, in which the addition of IL-2 used to induce T cell proliferation in vitro was partially compensating for the loss of effector function (56, 57). Importantly, subtle differences in CTL cytotoxicity using in vitro assays may be predictive of more serious cytotoxic defects in vivo, leading to poor immune responses (58). Therefore, the small differences in cytotoxicity we observed could have consequences in long-term antitumor immunity in patients.

We have previously shown in CD4 T cells that Apc silencing altered NFAT nuclear translocation and reduced NFAT-driven transcriptional activation, leading to impaired IL-2 gene expression. Furthermore, CD4 T cells from *Apc^{Min/+}* mice had reduced capacity to produce IL-2, IL-4, and IFN- γ . Finally, Tregs in these mutant mice showed impaired differentiation and production of the anti-inflammatory cytokine IL-10 (29). We show in this study that CTLs from *Apc^{Min/+}* mice also had an impaired capacity to translocate NFATc2 to the nucleus. Interestingly, NFATc2 formed microclusters associated with microtubules in CD8 T cells (data not shown), as we previously showed in CD4 T cells (29). The total number of CD3⁺ lymphocytes, CD3⁺CD4⁺ or CD3⁺CD8⁺ was not reduced in *Apc^{Min/+}* mice but even increased starting from 10 wk of age and stayed enhanced at 12 and 14 wk of age, at which time signs of polyposis become evident. This suggests that long-term survival in vivo of CD4 or CD8 lymphocytes is not impaired, but T cell stimulation due to intestinal inflammation at the appearance of polyposis may increase T cell numbers. Interestingly, the analysis of the expression of several differentiation markers (e.g., CD25, granzyme B, CD44, and CD62L) did not show activation of freshly isolated T cells from *Apc^{Min/+}* mice. In addition, ex vivo activation with ConA and IL-2 revealed only mildly altered CD44 and CD62L expression at day 2 and of granzyme B at day 6 in *Apc^{Min/+}* mice. Interestingly, under the same stimulation conditions, the differences in expression of CD44 and CD62L between *Apc^{Min/+}* and control T cells were more pronounced and significant in the CD4 T cell population. This was not accompanied by differences in the

proliferative capacity of CD4 and CD8 T cells under the same stimulatory conditions. This is, in part, in contrast with our previous data on lamina propria CD4 T cells that displayed impaired proliferation capacity at suboptimal stimulation (29). The differences may be due to the distinct tissue origin of T cells, lamina propria in our previous publication and spleen and lymph nodes in this study, or they may be due to the different stimulatory conditions used, different doses of CD3/CD28 on lamina propria cells in our previous work versus ConA in this study. In addition, Apc-silenced human and *Apc^{Min/+}* mouse ex vivo-differentiated CTLs produced an equal amount of IL-2, TNF- α , and IFN- γ after restimulation with CD3/CD28 Abs. Therefore, in comparison with our previous work (29), CD8 T cells appear to be less sensitive to Apc defects than CD4 T cells when performing their activation programs leading to differentiation and production of cytokines. Furthermore, the intestinal environment in *Apc^{Min/+}* mice could also influence these responses.

Altogether, the data presented in this study show that Apc is involved in the regulation of CTL effector functions that drive target cell killing. Hence, Apc defects impair both actin and microtubule cytoskeleton remodeling at the immunological synapse, centrosome polarization and lytic granule dynamics, targeting, and fusion at the synapse. However, CD8 T cell differentiation and cytokine production appear much less dependent on Apc compared with what has been observed in CD4 T cells (29). Thus, Apc defects may not significantly alter the acquisition of effector functions in CD8 T cells but impair the CTL capacities to kill tumor cells and could therefore have an impact in long-term antitumor immune responses in familial adenomatous polyposis patients, allowing easier tumor escape.

DISCLOSURES

The authors have no financial conflicts of interest.

ACKNOWLEDGMENTS

We thank Drs. F. Sepulveda and D. Scott-Algara for scientific advice, J.Y. Tinevez, A. Salles, J. Fernandes and the Unit of Technology and Service Photonic BioImaging facility, Institut Pasteur for technical support and the ICAREB Biological Resources core facility team, Institut Pasteur for providing primary T cell samples. We are grateful to I. N athke for Abs.

REFERENCES

- Huse, M., E. J. Quann, and M. M. Davis. 2008. Shouts, whispers and the kiss of death: directional secretion in T cells. *Nat. Immunol.* 9: 1105–1111.
- Soares, H., R. Lasserre, and A. Alcover. 2013. Orchestrating cytoskeleton and intracellular vesicle traffic to build functional immunological synapses. *Immunol. Rev.* 256: 118–132.
- Kupfer, A., and G. Dennert. 1984. Reorientation of the microtubule-organizing center and the Golgi apparatus in cloned cytotoxic lymphocytes triggered by binding to lysable target cells. *J. Immunol.* 133: 2762–2766.
- Kupfer, A., T. R. Mosmann, and H. Kupfer. 1991. Polarized expression of cytokines in cell conjugates of helper T cells and splenic B cells. *Proc. Natl. Acad. Sci. USA* 88: 775–779.
- Depoil, D., R. Zaru, M. Guiraud, A. Chauveau, J. Harriague, G. Bismuth, C. Utzny, S. M uller, and S. Valitutti. 2005. Immunological synapses are versatile structures enabling selective T cell polarization. *Immunity* 22: 185–194.
- Ritter, A. T., Y. Asano, J. C. Stinchcombe, N. M. Dieckmann, B. C. Chen, C. Gawden-Bone, S. van Engelenburg, W. Legant, L. Gao, M. W. Davidson, et al. 2015. Actin depletion initiates events leading to granule secretion at the immunological synapse. *Immunity* 42: 864–876.
- Stinchcombe, J. C., E. Majorovits, G. Bossi, S. Fuller, and G. M. Griffiths. 2006. Centrosome polarization delivers secretory granules to the immunological synapse. [Published erratum appears in 2006 *Nature* 444: 236.] *Nature* 443: 462–465.
- Dieckmann, N. M., G. L. Frazer, Y. Asano, J. C. Stinchcombe, and G. M. Griffiths. 2016. The cytotoxic T lymphocyte immune synapse at a glance. *J. Cell Sci.* 129: 2881–2886.
- Ritter, A. T., S. M. Kapnick, S. Murugesan, P. L. Schwartzberg, G. M. Griffiths, and J. Lippincott-Schwartz. 2017. Cortical actin recovery at the immunological synapse leads to termination of lytic granule secretion in cytotoxic T lymphocytes. *Proc. Natl. Acad. Sci. USA* 114: E6585–E6594.
- Rodr iguez-Boulan, E., and I. G. Macara. 2014. Organization and execution of the epithelial polarity programme. *Nat. Rev. Mol. Cell Biol.* 15: 225–242.
- Elric, J., and S. Etienne-Manneville. 2014. Centrosome positioning in polarized cells: common themes and variations. *Exp. Cell Res.* 328: 240–248.
- Ludford-Menting, M. J., J. Oliaro, F. Sacirbegovic, E. T. Cheah, N. Pedersen, S. J. Thomas, A. Pasam, R. Iazzolino, L. E. Dow, N. J. Waterhouse, et al. 2005. A network of PDZ-containing proteins regulates T cell polarity and morphology during migration and immunological synapse formation. *Immunity* 22: 737–748.
- Real, E., S. Faure, E. Donnadieu, and J. Delon. 2007. Cutting edge: atypical PKCs regulate T lymphocyte polarity and scanning behavior. *J. Immunol.* 179: 5649–5652.
- Lasserre, R., S. Charrin, C. Cuche, A. Danckaert, M. I. Thoulouze, F. de Chaumont, T. Duong, N. Perrault, N. Varin-Blank, J. C. Olivo-Marin, et al. 2010. Ezrin tunes T-cell activation by controlling Dlg1 and microtubule positioning at the immunological synapse. *EMBO J.* 29: 2301–2314.
- Bertrand, F., M. Esquerr e, A. E. Petit, M. Rodrigues, S. Duchez, J. Delon, and S. Valitutti. 2010. Activation of the ancestral polarity regulator protein kinase C zeta at the immunological synapse drives polarization of Th cell secretory machinery toward APCs. *J. Immunol.* 185: 2887–2894.
- Xavier, R., S. Rabizadeh, K. Ishiguro, N. Andre, J. B. Ortiz, H. Wachtel, D. G. Morris, M. Lopez-Illasaca, A. C. Shaw, W. Swat, and B. Seed. 2004. Discs large (Dlg1) complexes in lymphocyte activation. *J. Cell Biol.* 166: 173–178.
- Round, J. L., L. A. Humphries, T. Tomassian, P. Mittelstadt, M. Zhang, and M. C. Miceli. 2007. Scaffold protein Dlg1 coordinates alternative p38 kinase activation, directing T cell receptor signals toward NFAT but not NF-kappaB transcription factors. *Nat. Immunol.* 8: 154–161.
- McCartney, B. M., and I. S. N athke. 2008. Cell regulation by the Apc protein Apc as master regulator of epithelia. *Curr. Opin. Cell Biol.* 20: 186–193.
- Zeineldin, M., and K. L. Neufeld. 2013. More than two decades of Apc modeling in rodents. *Biochim. Biophys. Acta* 1836: 80–89.
- Su, L. K., K. W. Kinzler, B. Vogelstein, A. C. Preisinger, A. R. Moser, C. Luongo, K. A. Gould, and W. F. Dove. 1992. Multiple intestinal neoplasia caused by a mutation in the murine homolog of the APC gene. *Science* 256: 668–670.
- Moser, A. R., H. C. Pitot, and W. F. Dove. 1990. A dominant mutation that predisposes to multiple intestinal neoplasia in the mouse. *Science* 247: 322–324.
- Nelson, S., and I. S. N athke. 2013. Interactions and functions of the adenomatous polyposis coli (APC) protein at a glance. *J. Cell Sci.* 126: 873–877.

23. Etienne-Manneville, S. 2009. APC in cell migration. *Adv. Exp. Med. Biol.* 656: 30–40.
24. Bérout, C., and T. Soussi. 1996. APC gene: database of germline and somatic mutations in human tumors and cell lines. *Nucleic Acids Res.* 24: 121–124.
25. Gounaris, E., N. R. Blatner, K. Dennis, F. Magnusson, M. F. Gurish, T. B. Strom, P. Beckhove, F. Gounari, and K. Khazaie. 2009. T-regulatory cells shift from a protective anti-inflammatory to a cancer-promoting proinflammatory phenotype in polyposis. *Cancer Res.* 69: 5490–5497.
26. Chae, W. J., and A. L. Bothwell. 2015. Spontaneous intestinal tumorigenesis in Apc (*Min*⁺) mice requires altered T cell development with IL-17a. *J. Immunol. Res.* 2015: 860106.
27. Akeus, P., V. Langenes, A. von Mentzer, U. Yrlid, Å. Sjöling, P. Saksena, S. Raghavan, and M. Quiding-Järbrink. 2014. Altered chemokine production and accumulation of regulatory T cells in intestinal adenomas of APC(*Min*⁺) mice. *Cancer Immunol. Immunother.* 63: 807–819.
28. Tanner, S. M., J. G. Daft, S. A. Hill, C. A. Martin, and R. G. Lorenz. 2016. Altered T-cell balance in lymphoid organs of a mouse model of colorectal cancer. *J. Histochem. Cytochem.* 64: 753–767.
29. Agüera-González, S., O. T. Burton, E. Vázquez-Chávez, C. Cucho, F. Herit, J. Bouchet, R. Lasserre, I. Del Río-Iñiguez, V. Di Bartolo, and A. Alcover. 2017. Adenomatous polyposis coli defines treg differentiation and anti-inflammatory function through microtubule-mediated NFAT localization. *Cell Rep.* 21: 181–194.
30. Rubtsov, Y. P., J. P. Rasmussen, E. Y. Chi, J. Fontenot, L. Castelli, X. Ye, P. Treuting, L. Siewe, A. Roers, W. R. Henderson, Jr., et al. 2008. Regulatory T cell-derived interleukin-10 limits inflammation at environmental interfaces. *Immunity* 28: 546–558.
31. Martínez, G. J., R. M. Pereira, T. Åijö, E. Y. Kim, F. Marangoni, M. E. Pipkin, S. Togher, V. Heissmeyer, Y. C. Zhang, S. Crotty, et al. 2015. The transcription factor NFAT promotes exhaustion of activated CD8⁺ T cells. *Immunity* 42: 265–278.
32. Schindelin, J., I. Arganda-Carreras, E. Frise, V. Kaynig, M. Longair, T. Pietzsch, S. Preibisch, C. Rueden, S. Saalfeld, B. Schmid, et al. 2012. Fiji: an open-source platform for biological-image analysis. *Nat. Methods* 9: 676–682.
33. Tinevez, J. Y., N. Perry, J. Schindelin, G. M. Hoopes, G. D. Reynolds, E. Laplantine, S. Y. Bednarek, S. L. Shorte, and K. W. Eliceiri. 2017. TrackMate: an open and extensible platform for single-particle tracking. *Methods* 115: 80–90.
34. Edelstein, A. D., M. A. Tsuchida, N. Amodaj, H. Pinkard, R. D. Vale, and N. Stuurman. 2014. Advanced methods of microscope control using µManager software. *J. Biol. Methods* 1: e10.
35. Kamsma, D., P. Bochet, F. Oswald, N. Alblas, S. Goyard, G. J. L. Wuite, E. J. G. Peterman, and T. Rose. 2018. Single-cell acoustic force spectroscopy: resolving kinetics and strength of T cell adhesion to fibronectin. *Cell Rep.* 24: 3008–3016.
36. Näthke, I. S., C. L. Adams, P. Polakis, J. H. Sellin, and W. J. Nelson. 1996. The adenomatous polyposis coli tumor suppressor protein localizes to plasma membrane sites involved in active cell migration. *J. Cell Biol.* 134: 165–179.
37. Li, Z., K. Kroboth, I. P. Newton, and I. S. Näthke. 2008. Novel self-association of the APC molecule affects APC clusters and cell migration. *J. Cell Sci.* 121: 1916–1925.
38. Etienne-Manneville, S. 2013. Microtubules in cell migration. *Annu. Rev. Cell Dev. Biol.* 29: 471–499.
39. Etienne-Manneville, S., and A. Hall. 2003. Cdc42 regulates GSK-3beta and adenomatous polyposis coli to control cell polarity. *Nature* 421: 753–756.
40. Etienne-Manneville, S., J. B. Manneville, S. Nicholls, M. A. Ferenczi, and A. Hall. 2005. Cdc42 and Par6-PKCzeta regulate the spatially localized association of Dlg1 and APC to control cell polarization. *J. Cell Biol.* 170: 895–901.
41. Okada, K., F. Bartolini, A. M. Deaconescu, J. B. Moseley, Z. Dogic, N. Grigorieff, G. G. Gundersen, and B. L. Goode. 2010. Adenomatous polyposis coli protein nucleates actin assembly and synergizes with the formin mDial. *J. Cell Biol.* 189: 1087–1096.
42. Juanes, M. A., H. Bouguenina, J. A. Eskin, R. Jaiswal, A. Badache, and B. L. Goode. 2017. Adenomatous polyposis coli nucleates actin assembly to drive cell migration and microtubule-induced focal adhesion turnover. *J. Cell Biol.* 216: 2859–2875.
43. Le Floc’h, A., Y. Tanaka, N. S. Bantilan, G. Voisinne, G. Altan-Bonnet, Y. Fukui, and M. Huse. 2013. Annular PIP3 accumulation controls actin architecture and modulates cytotoxicity at the immunological synapse. [Published erratum appears in 2017 *J. Exp. Med.* 214: 1203.] *J. Exp. Med.* 210: 2721–2737.
44. Bryceson, Y. T., C. Fauriat, J. M. Nunes, S. M. Wood, N. K. Björkström, E. O. Long, and H. G. Ljunggren. 2010. Functional analysis of human NK cells by flow cytometry. *Methods Mol. Biol.* 612: 335–352.
45. De Meester, J., R. Calvez, S. Valitutti, and L. Dupré. 2010. The Wiskott-Aldrich syndrome protein regulates CTL cytotoxicity and is required for efficient killing of B cell lymphoma targets. *J. Leukoc. Biol.* 88: 1031–1040.
46. Lasserre, R., and A. Alcover. 2010. Cytoskeletal cross-talk in the control of T cell antigen receptor signaling. *FEBS Lett.* 584: 4845–4850.
47. Bouchet, J., I. Del Río-Iñiguez, R. Lasserre, S. Agüera-Gonzalez, C. Cucho, A. Danckaert, M. W. McCaffrey, V. Di Bartolo, and A. Alcover. 2016. Rac1-Rab11-FIP3 regulatory hub coordinates vesicle traffic with actin remodeling and T-cell activation. *EMBO J.* 35: 1160–1174.
48. Osmani, N., N. Vitale, J. P. Borg, and S. Etienne-Manneville. 2006. Scrib controls Cdc42 localization and activity to promote cell polarization during astrocyte migration. *Curr. Biol.* 16: 2395–2405.
49. Gomez, T. S., K. Kumar, R. B. Medeiros, Y. Shimizu, P. J. Leibson, and D. D. Billadeau. 2007. Formins regulate the actin-related protein 2/3 complex-independent polarization of the centrosome to the immunological synapse. *Immunity* 26: 177–190.
50. Stowers, L., D. Yelon, L. J. Berg, and J. Chant. 1995. Regulation of the polarization of T cells toward antigen-presenting cells by Ras-related GTPase CDC42. *Proc. Natl. Acad. Sci. USA* 92: 5027–5031.
51. Burkhardt, J. K., J. M. McIlvain, Jr., M. P. Sheetz, and Y. Argon. 1993. Lytic granules from cytotoxic T cells exhibit kinesin-dependent motility on microtubules in vitro. *J. Cell Sci.* 104: 151–162.
52. Kurowska, M., N. Goudin, N. T. Nehme, M. Court, J. Garin, A. Fischer, G. de Saint Basile, and G. Ménasché. 2012. Terminal transport of lytic granules to the immune synapse is mediated by the kinesin-1/Slp3/Rab27a complex. *Blood* 119: 3879–3889.
53. Wolint, P., M. R. Betts, R. A. Koup, and A. Oxenius. 2004. Immediate cytotoxicity but not degranulation distinguishes effector and memory subsets of CD8⁺ T cells. *J. Exp. Med.* 199: 925–936.
54. Houmadi, R., D. Guipouy, J. Rey-Barroso, Z. Vasconcelos, J. Cornet, M. Manghi, N. Destainville, S. Valitutti, S. Allart, and L. Dupré. 2018. The wiskott-aldrich syndrome protein contributes to the assembly of the LFA-1 nanocluster belt at the lytic synapse. *Cell Rep.* 22: 979–991.
55. Moser, A. R., A. R. Shoemaker, C. S. Connelly, L. Clipson, K. A. Gould, C. Luongo, W. F. Dove, P. H. Siggers, and R. L. Gardner. 1995. Homozygosity for the *Min* allele of *Apc* results in disruption of mouse development prior to gastrulation. *Dev. Dyn.* 203: 422–433.
56. Hackmann, Y., S. C. Graham, S. Ehl, S. Höning, K. Lehmborg, M. Aricò, D. J. Owen, and G. M. Griffiths. 2013. Syntaxin binding mechanism and disease-causing mutations in *Munc18-2*. *Proc. Natl. Acad. Sci. USA* 110: E4482–E4491.
57. Bryceson, Y. T., E. Rudd, C. Zheng, J. Edner, D. Ma, S. M. Wood, A. G. Bechensteen, J. J. Boelens, T. Celkan, R. A. Farah, et al. 2007. Defective cytotoxic lymphocyte degranulation in syntaxin-11 deficient familial hemophagocytic lymphohistiocytosis 4 (FHL4) patients. *Blood* 110: 1906–1915.
58. Jessen, B., A. Maul-Pavicic, H. Ufheil, T. Vraetz, A. Enders, K. Lehmborg, A. Längler, U. Gross-Wieltsch, A. Bay, Z. Kaya, et al. 2011. Subtle differences in CTL cytotoxicity determine susceptibility to hemophagocytic lymphohistiocytosis in mice and humans with Chediak-Higashi syndrome. *Blood* 118: 4620–4629.